



HAL
open science

Auroral electron distributions within and close to the Saturn kilometric radiation source region

Patricia Schippers, Christopher S. Arridge, J. Menietti, Donald A. Gurnett, Laurent Lamy, Baptiste Cecconi, Donald G. Mitchell, Nicolas André, William S. Kurth, S. Grimald, et al.

► **To cite this version:**

Patricia Schippers, Christopher S. Arridge, J. Menietti, Donald A. Gurnett, Laurent Lamy, et al.. Auroral electron distributions within and close to the Saturn kilometric radiation source region. *Journal of Geophysical Research Space Physics*, 2011, 116, pp.05203. 10.1029/2011JA016461 . hal-03733244

HAL Id: hal-03733244

<https://hal.science/hal-03733244>

Submitted on 22 Aug 2022

HAL is a multi-disciplinary open access archive for the deposit and dissemination of scientific research documents, whether they are published or not. The documents may come from teaching and research institutions in France or abroad, or from public or private research centers.

L'archive ouverte pluridisciplinaire **HAL**, est destinée au dépôt et à la diffusion de documents scientifiques de niveau recherche, publiés ou non, émanant des établissements d'enseignement et de recherche français ou étrangers, des laboratoires publics ou privés.

Copyright

Auroral electron distributions within and close to the Saturn kilometric radiation source region

P. Schippers,¹ C. S. Arridge,^{2,3} J. D. Menietti,¹ D. A. Gurnett,¹ L. Lamy,^{4,5} B. Cecconi,⁵ D. G. Mitchell,⁶ N. André,^{7,8} W. S. Kurth,¹ S. Grimald,^{7,8} M. K. Dougherty,⁴ A. J. Coates,^{2,3} N. Krupp,⁹ and D. T. Young¹⁰

Received 9 January 2011; revised 9 February 2011; accepted 21 February 2011; published 10 May 2011.

[1] On 17 October 2008, Cassini observed for the first time the electron populations associated with the crossing of a Saturn kilometric radiation source region and its surroundings. These observations allow for the first time the constraint and quantification of the high-latitude acceleration processes, the current systems, and the origin of the low-frequency electromagnetic waves. Enhanced fluxes of field-aligned energetic electrons were measured by the Cassini electron plasma spectrometer in conjunction with unusual intense field-aligned current systems identified using the magnetometer instrument. In the region where downward field-aligned currents were measured, electron data show evidence of two types of upward accelerated electron beams: a broadband energetic (1–100 keV) electron population that is observed throughout the region and a narrow-banded (0.1–1 keV) electron population that is observed sporadically. In the regions where the magnetic field signatures showed evidence for upward field-aligned currents, we observe electron loss cone distributions and some evidence of shell-like distributions. Such nonthermal electron populations are commonly known as a potential free energy source to drive plasma instabilities. In the downward current region, the low-energy and energetic beams are likely the source of the very low frequency emissions. In the upward current region, the shell distribution is identified as a potential source for Saturn kilometric radiation generation via the cyclotron maser instability.

Citation: Schippers, P., et al. (2011), Auroral electron distributions within and close to the Saturn kilometric radiation source region, *J. Geophys. Res.*, 116, A05203, doi:10.1029/2011JA016461.

1. Introduction

[2] Since 2004, the Cassini spacecraft has been exploring the Saturnian magnetosphere at both equatorial and high latitudes. Cassini is unique in providing the first repeated sampling of the high-latitude and polar regions of a rapidly rotating magnetosphere. During a crossing of high-latitude

auroral magnetic field lines during 17 October 2008, the radio and plasma wave science (RPWS) instrument onboard Cassini measured intense kilometric radio emissions (known as Saturn kilometric radiation, SKR) at frequencies close to and even below the electron cyclotron frequency, consistent with in situ observations of the SKR source region [Lamy *et al.*, 2010; Kurth *et al.*, 2011]. SKR is thought to be generated by the same plasma instability that generates terrestrial auroral kilometric radiation (AKR) and thus these observations provide a unique opportunity to analyze the role of electrons as a source of the cyclotron maser instability in a wider planetary and astrophysical context [e.g., Ergun *et al.*, 2000].

[3] In the terrestrial magnetosphere, the properties of the source region of AKR have been studied and analyzed using in situ observations from several spacecraft, combined with remote observations. The cyclotron maser instability (CMI) [Wu and Lee, 1979; Pritchett and Strangeway, 1985] is the favored generation mechanism for AKR and relies on a positive $\partial f / \partial v_{\perp}$ slope in the electron distribution function. The unambiguous identification of such nonthermal signatures in in situ particle data and their ability to generate AKR via the CMI has been the subject of considerable research over the last 30 years. This task is difficult because (1) a number of

¹Department of Physics and Astronomy, University of Iowa, Iowa City, Iowa, USA.

²Mullard Space Science Laboratory, University College London, Holmbury St. Mary, UK.

³Centre for Planetary Sciences at UCL/Birkbeck, London, WC1E 6BT, UK.

⁴Department of Space and Atmospheric Physics, Imperial College, London, UK.

⁵LESIA, CNRS, Observatoire de Meudon, Meudon, France.

⁶Applied Physics Laboratory, Johns Hopkins University, Laurel, Maryland, USA.

⁷Centre d'Étude Spatiale des Rayonnements, Université de Toulouse, UPS, Toulouse, France.

⁸CNRS UMR 5187, Toulouse, France.

⁹Max-Planck-Institut für Sonnensystemforschung, Katlenburg-Lindau, Germany.

¹⁰Southwest Research Institute, San Antonio, Texas, USA.

features in the electron distribution (such as loss cones and trapped populations) can produce $\partial f/\partial v_{\perp} > 0$ and so one needs to identify which feature produces the largest growth rate, and (2) wave-particle interactions (WPIs) rapidly modify the observed distributions and smooth out the initial nonthermal feature that provides the free-energy source to drive the waves. The latter point implies that plasma instrumentation with a very high temporal cadence are required to observe the nonthermal features at the origin of the waves.

[4] Viking was among the first missions dedicated to the study of the magnetospheric plasma in the auroral acceleration region and provided the first in situ measurements of particle distributions (20 s resolution) in and close to the AKR source region [Benson and Calvert, 1979; Ungstrup et al., 1990; Louarn et al., 1990; Roux et al., 1993]. These analyses showed that (1) the cold electron density drops inside the source region, (2) an enhanced loss cone phase space distribution is present close to the AKR region and the loss cone is filled inside the source region, (3) an upward ion beam of several keV is present, indicating a potential drop of a few kV below the spacecraft, and (4) the magnetic field data are consistent with upward field-aligned currents in the source region. Roux et al. [1993] discussed three main nonthermal features in the distribution that could drive waves: loss cones, phase space “holes,” and trapped electron populations. In the latter case of a trapped electron population the hot plasma must be dominant. Roux et al. [1993] argued that the presence of cold plasma cavities and trapped electrons supported the latter as the principal free energy source. Observations from Dynamics Explorer 1 (6 s resolution) at slightly larger altitudes just beyond the auroral acceleration region largely supported the findings from Viking [Meniotti et al., 1993]. However, in most cases rapid temporal and/or spatial variations precluded the measurement of reliable electron distributions from the AKR source region and in many cases a strong modification of the electron distribution by wave-particle interactions was observed, typically including perpendicular electron heating [Morgan et al., 2000] and loss cone filling [Ungstrup et al., 1990].

[5] To remedy this, the Fast Auroral Snapshot (FAST) mission was designed to make high-resolution measurements (30 ms) of electric fields, radio emissions and particles in Earth’s high-latitude auroral region. A series of orbits led to a comprehensive multi-instrument analysis of the upward current regions [Elphic et al., 1998; Ergun et al., 2002], downward current regions [Carlson et al., 1998; Elphic et al., 1998], and the AKR source region [Delory et al., 1998; Ergun et al., 1998]. The presence of deep plasma density cavities in the AKR source region, as reported by ISIS 1, DE 1 and Viking, was also confirmed [Strangeway et al., 1998]. Regarding the electron distributions in the AKR source region, broad plateaus over a wide range of pitch angles were observed in auroral electron distributions [Delory et al., 1998], indicative of the stabilization of these distributions by WPIs with AKR. Finally, Ergun et al. [2000] demonstrated that a “shell” or “horseshoe” distribution is more efficient to generate AKR than a loss cone distribution.

[6] At Saturn, the very first observation of an SKR source crossing region on 17 October 2008 is an opportunity to undertake a comparison study between the auroral kilometeric radiation at Earth and at Saturn [Lamy et al., 2010; Kurth et al., 2011]. This unique interval has been discussed

on some aspects such as the overall nature of the interval [Kurth et al., 2011; Lamy et al., 2010] including a discussion on its relationship to magnetospheric dynamics [Bunce et al., 2010], the SKR polarization properties [Lamy et al., 2011], the instability source mechanisms [Mutel et al., 2010], and the low-frequency waves [Kopf et al., 2010].

[7] The first results reported on this event described unusual field-aligned current signatures and the enhancement of SKR intensity with frequency dropping close to and below the local electron gyrofrequency [Lamy et al., 2010; Bunce et al., 2010]. Sources of SKR were identified in the upward current region, at a planetocentric radial distance of $5 R_S$ (equatorial radius of Saturn, 60268 km) in the midnight sector at dipole L shells between 25 and 30, embedded in hot plasma [Lamy et al., 2010; Kurth et al., 2011]. A spiral-shaped auroral oval, consistent with a solar wind compression and nightside injection was reported [Lamy et al., 2010; Bunce et al., 2010]. The SKR generation is consistent with radio waves amplified at a large wave normal angle by hot electrons (6–9 keV) through the CMI [Lamy et al., 2010]. Additional features such as energetic upward ions [Kurth et al., 2011] measured by the MIMI/INCA instrument (Magnetospheric Imaging Instrument/Ion neutral Camera; Krimigis et al. [2004]), and low-frequency wave activity enhancement associated with electron beams [Kopf et al., 2010] were observed in the source region.

[8] In this paper we discuss details of the electron distributions measured by the Cassini Plasma Spectrometer Electron Spectrometer (CAPS/ELS) and Low Energy Magnetospheric Measurement System (LEMMS) instruments in vicinity and inside the SKR source region. We relate the measured electron distributions to simultaneously observed field-aligned currents and wave activity. In section 2, we describe the CAPS/ELS instrument and present an overview of the multi-instrument data (RPWS, CAPS/ELS, CAPS/IMS, and MAG). In sections 3 and 4, we discuss the electron observations in the downward/upward current region, respectively: their energy and angular distributions (sections 3.1, 3.2, and 4.1), the associated ion distributions (sections 3.3 and 4.2), the inferred characteristics of the acceleration source (sections 3.4 and 4.3), the wave-particle interactions (sections 3.5 and 4.5), and the cold electron density in the upward current region (section 4.4). In section 5, we conclude with a summary sketch of the apparent spacecraft trajectory through the different acceleration regions, inferred from the multi-instrument data analysis in sections 3 and 4.

2. Instrumentation and Data

2.1. Instrumentation

[9] The CAPS/ELS instrument [Linder et al., 1998; Young et al., 2004] is a top hat electrostatic analyzer which measures electron count rates from 0.56 eV to 28.25 keV in 63 contiguous quasi-logarithmically spaced energy channels with an energy resolution $\Delta E/E$ of 16.9%. The eight anodes of the instrument provide an instantaneous field of view of 160° by 5.2° . To increase this field of view, the instrument is mounted on a turntable, known as the actuator, which sweeps the anodes around the Z axis of the spacecraft and provides a spatial coverage of 160° in elevation and 208° in azimuth. The actuator rotates at around one degree of azimuth per second covering just over 2π sr of the sky in about 3 min.

However, anodes 1 and 8 are partially obscured by parts of the Cassini spacecraft, particularly at extreme actuation (azimuth) angles and are generally not used.

[10] During the particular period of interest, the spacecraft attitude and instrument actuation limits provided good coverage of the antiparallel (180°) pitch angle but the parallel direction (0°) was poorly covered and viewing was typically limited to pitch angles larger than 20° . As the spacecraft crossed the Southern Hemisphere, the parallel and antiparallel directions correspond to the downward and the upward directions, respectively.

[11] For this study pitch angle distributions were generated at two different cadences. To resolve the large-scale structure, wide pitch angle coverage is clearly advantageous and so pitch angle distributions were obtained by integrating the observations over a full 3 min sweep of the actuator. This is also advantageous for the accurate subtraction of the instrument background [Arridge *et al.*, 2009]. However, as was discovered by terrestrial auroral missions, the auroral electron distributions can be rapidly modified by WPIs and so 3 min integrations would typically preclude observation of unstable features in the distribution. Indeed, stabilization of the electron distributions due to growth of AKR were observed to occur on a timescale of the order of 1 ms [Wu *et al.*, 1982; Delory *et al.*, 1998], much faster than the analyzer measurement rate. In addition, transient beams and loss cones would also be smoothed. So we also used the highest resolution data (2s) to resolve the very fine electron structures. The disadvantage of this approach is the limited pitch angle coverage and poor removal of the instrument background. In the identification of $\partial f/\partial v_{\parallel} > 0$ and $\partial f/\partial v_{\perp} > 0$ regions in the auroral electron distributions, care was taken to properly treat the background and noise level issues in the particle data.

[12] The Cassini ion mass spectrometer CAPS/IMS instrument [Young *et al.*, 2004] is a top hat electrostatic analyzer which measures ion count rates from 1 eV to 50280 eV in 63 energy channels with an energy resolution $\Delta E/E$ of 16.9% and a mass resolution of $M/\Delta M \simeq 70$. The eight anodes of the instrument provide an instantaneous field of view of 160° by 8.3° . The instrument is mounted on the actuator, in parallel with CAPS/ELS. The highest-resolution ion data are at a cadence of 4 s with the largest field of view covered in approximately 3 min similar to ELS.

[13] The magnetometer (MAG) experiment [Dougherty *et al.*, 2004] includes a fluxgate magnetometer which measures magnetic field data at a maximum cadence of 31 ms. In this paper, data averaged to a 1 min cadence are used for the large-scale analysis of section 2.

[14] The RPWS experiment [Gurnett *et al.*, 2004] measures electric fields using three nearly orthogonal antennas from 1 Hz to 16 MHz. The signal is processed by receiver systems covering different frequency ranges. In this study we show the measurements of the medium frequency receiver (bandwidth from 24 Hz to 12 kHz, shown above 400 Hz) and the high-frequency receiver (bandwidth from 3.5 kHz to 16 MHz).

2.2. Large-Scale Data Analysis

[15] Figure 1 summarizes the electron, magnetometer, and radio and plasma wave observations between 0600 and 0930 UT on 17 October 2008. Figure 1a displays the electric wave spectrogram measured by the RPWS instrument. At

high frequencies (10–1000 kHz) the broadband SKR frequency envelope is observed to decrease until 0900 UT [Lamy *et al.*, 2010; Kurth *et al.*, 2011]. Its intensity is enhanced at 0800 UT and its lower cutoff frequency reaches the electron cyclotron frequency (f_{ce}) represented by the white line and determined from the observed magnetic field strength. At very low frequencies, the wave activity is characterized by enhancements below 4000 Hz from 0715 UT to 0745 UT and from 0800 UT to 0915 UT, identified as broadband electrostatic noise and whistler mode auroral hiss emissions by Kopf *et al.* [2010].

[16] Figures 1b–1d display the electron differential energy flux as a function of energy as measured by CAPS/ELS in three different pitch angle bins: 20° (downward), 90° (perpendicular) and 180° (upward). These fluxes have been calculated from a 3 min integration over one actuator sweep to give the fullest pitch angle distribution possible. However, gaps do exist and periods with no pitch angle coverage are gray. Fluxes below around 10 eV are trapped spacecraft photoelectrons.

[17] Figure 1e presents the normalized electron flux at 3.9 keV as a function of time and pitch angle.

[18] Figure 1f shows the electron number density (corrected for the positive spacecraft potential), where black is the total density, red is the hot electron density (400–28,000 eV), orange is the warm electron density (50–400 eV) and blue is the cold electron density (0.5–50 eV). A full set of electron moments (density and parallel and perpendicular electron temperatures) was derived. The derivation method is described in Appendix A, and the moment profiles are presented in Figure A1.

[19] Figure 1g presents the azimuthal B_ϕ component of the magnetic field, where gradients in this component indicate the presence of field-aligned currents [Bunce *et al.*, 2010; Talboys *et al.*, 2009a; Lamy *et al.*, 2010; Kurth *et al.*, 2011]. Positive (negative) gradients indicate upward (downward) field-aligned currents, highlighted by the horizontal lines in red (blue).

[20] The magnetometer data (Figure 1g) show the presence of an upward field-aligned current region between 0620 and 0640 UT and a downward current region between 0640 and 0748 UT. This system of field-aligned currents is similar to the typical set of current systems observed in Saturn's high-latitude magnetosphere in the predusk Northern Hemisphere [Talboys *et al.*, 2009a] except the lagging magnetic field configuration turning into a leading configuration in the second part of the downward current region. These are then followed by another large "unusual" upward current region extending until 0900 UT where Bunce *et al.* [2010] inferred that the spacecraft crossed the open-closed field line boundary. This upward current region includes smaller features of downward currents at about 0840 UT and 0850 UT. No significant electron anisotropies can be identified in the electron data in the first region of upward current (0620–0640 UT), suggesting that the thermal electron current [Knight, 1973] is carrying the bulk of the observed current and that any acceleration regions are below the spacecraft. In the downward current region (0640–0748 UT) a hot beam of keV electrons with a narrow pitch angle distribution in the upward direction is observed. In the second upward current region (0748–0900 UT), the pitch angle distribution is rather broad and shows evidence of both upward and downward moving

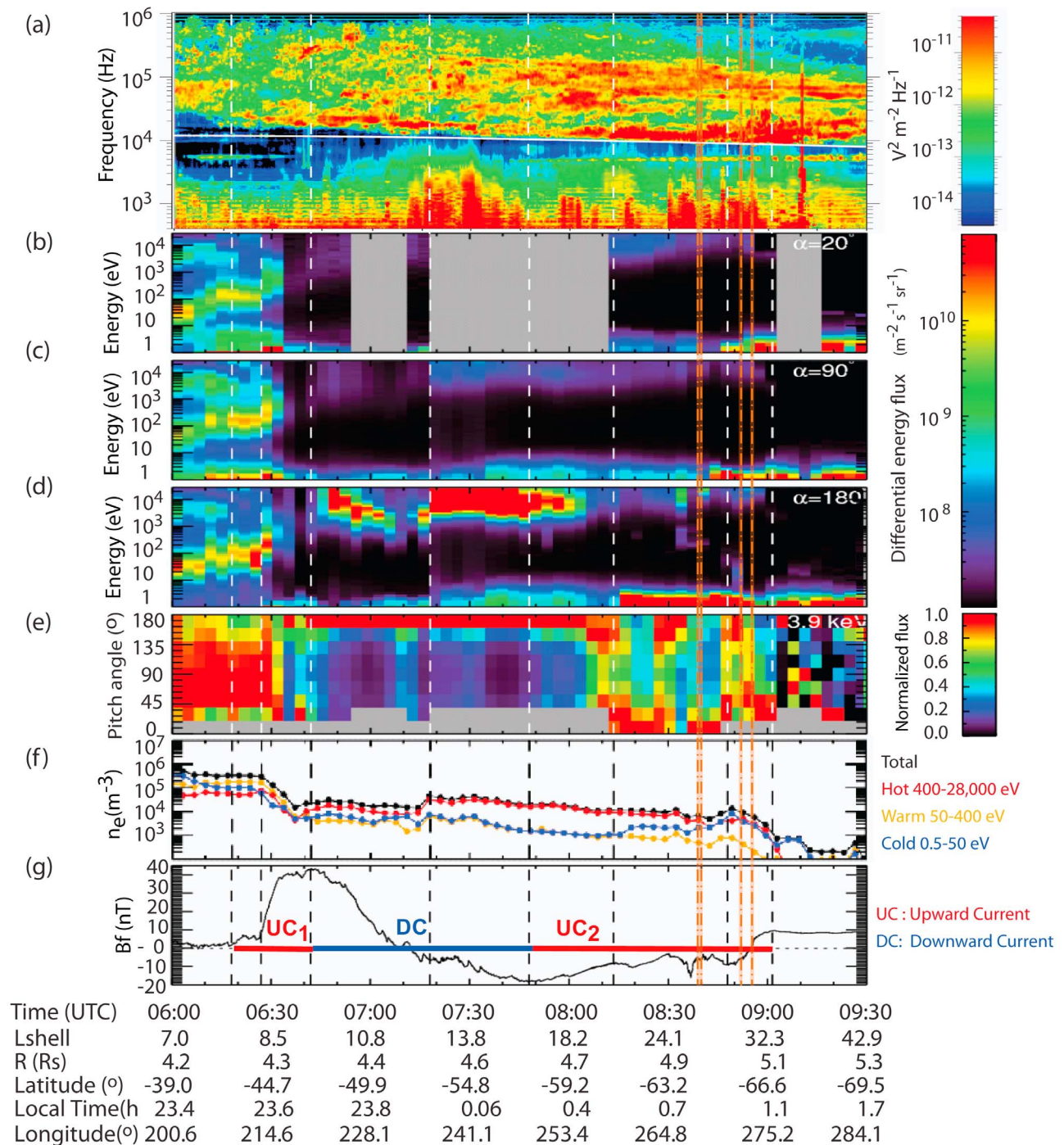


Figure 1. Multi-instrument view of the event on 17 October 2008 in the 0600–0930 UT time interval. (a) The RPWS spectrogram in the 400– 10^6 Hz frequency range. (b, c, and d) The three-dimensional CAPS/ELS energy-time spectrograms in the 20°, 90°, and 180° pitch angle directions, respectively. (e) The pitch angle distribution normalized at each time at 3.9 keV. (f) The total electron density (black), the cold (0.1–50 eV) electron density (blue), the warm (50–400 eV) electron density (orange), and the hot (0.4–28 keV) electron density (red). (g) The azimuthal component of the magnetic field measured by MAG. The orange dashed lines indicates the SKR source regions identified by *Lamy et al.* [2010].

electrons, sometimes coincident and consistent with small-scale downward current regions (see further details in section 4.1).

[21] From 0600 UT to 0630 UT, two magnetospheric electron populations are observed which broadly compare to the “thermal” (10–100 eV) and “suprathermal” (1–10 keV) populations identified by *Sittler et al.* [1983] and *Young et al.* [2005]. The thermal electron density dominates during this interval, during which the spacecraft crossed dipole L shells between 7 and 9, consistent with the equatorial observations. At the equator the thermal population is indeed generally observed inside of 15 R_S with a sharp gradient in density at 9 R_S and the flux of the suprathermal population decreases inward of 9 R_S inside Saturn’s neutral OH cloud [*Schippers et al.*, 2008]. The observations from high latitudes presented in Figure 1 show that the thermal population is typically field aligned and mostly bidirectional, whereas the suprathermal population is slightly peaked in the 90° pitch angle direction, consistent with adiabatic outward and inward transport, respectively [*Rymer et al.*, 2008], and slightly decreases in flux outward. The electron density is high, and the electrons are globally almost isotropic (the anisotropies identified above are opposite for the hot/suprathermal and warm/thermal electrons and thus are largely eliminated as determined by the moment integration.)

[22] Between 0630 and 0640 UT, the flux of both thermal and suprathermal populations drops by a factor of 100 to near background levels. The electron density similarly drops by more than an order of magnitude.

[23] From 0640 to 0717 UT, a very hot (> 2 keV) unidirectional and quasi-monoenergetic electron population appears in the upward (antiparallel) direction with differential energy fluxes in excess of 10^{10} eV m⁻² s⁻¹ sr⁻¹ eV⁻¹ (≈ 200 erg cm⁻² s⁻¹ sr⁻¹ eV⁻¹ or $\approx 2 \times 10^{-9}$ J m⁻² s⁻¹ sr⁻¹ eV⁻¹). The peak energy decreases from 10 to 1 keV during the interval. A perpendicular flux component is present, with an intensity at least 1000 times smaller than the parallel component.

[24] At 0717 UT, this population becomes more broadband both in energy and pitch angle, the transition occurring within a single 3 min actuation sweep. The perpendicular flux appears here 10 times higher than in the previous interval. Furthermore a uniform increase in count rate over all energy bins is observed at the beginning of this period which is indicative of very energetic electrons penetrating the instrument and increasing the noise level. At 0748 UT the intensity begins to drop and the observed distribution begins to narrow in energy. Some enhancements in the ≈ 100 eV energy range appear around 0733 UT (details in section 3.2). These upward directed electron populations are coincident with a significant increase in low-frequency wave emission (< 2 kHz) identified as whistler mode auroral hiss. It is also coincident with the downward current region as identified from the B_ϕ component of the magnetometer data, and actually extends slightly beyond this region into the second upward current region. The large asymmetries in pitch angle are also present in the moments as a strong temperature anisotropy of $T_{\parallel}/T_{\perp} \approx 10$.

[25] From 0815 to 0900 UT, a more tenuous hot, weakly bidirectional electron population is observed above several keV. This interval coincides with the crossing of the SKR

source region and the “unusual” upward current region. As stated previously, hot electrons were identified as the only possible source of free energy for driving the CMI mechanism. Enhancements of upward hot electron fluxes are observed, notably at 0835 UT, and in the upward electron fluxes at lower energies (< 1 keV). The lower energy fluxes have been shown to drive whistler mode auroral hiss emissions [*Kopf et al.*, 2010].

[26] After 0900 UT the fluxes measured by CAPS/ELS are at the instrument noise level indicating a highly rarefied plasma environment with densities less than 10^2 m⁻³, identified as a region of open field lines by *Bunce et al.* [2010].

3. Observations in the Downward Current Region

[27] Figure 2 displays high-resolution CAPS/ELS electron phase space density distributions (Figures 2a, 2b, and 2c) at three different times in the 0640–0745 UT time interval, the energy-time high-resolution electron spectrogram measured by anode 7 (Figure 2d), and the pitch angle coverage of this anode (Figure 2e). One can easily observe that anode 7 covers periodically (through the actuator motion) the antiparallel direction near 180°. The electron spectrogram (Figure 2d) is separated in three subregions (delineated by the black dotted vertical lines), according to the three different electron signatures observed in the downward current region. Subregion 1 (0640–0717 UT) is populated by an energetic population, from 0.1 to 1 keV, in a subcorotating layer as identified from a lagging magnetic field signature [*Bunce et al.*, 2010]. The peak energy is observed to decrease with time during the whole subregion. Figure 2a displays the phase space density in the antiparallel direction (covered by anode 7 at this time, in red) and in the perpendicular direction (in blue), at 07:00 UT.

[28] Subregion 2 (0717–0733 UT) is populated by a more broadband, intense and energetic population, observed between 1 and 10 keV in the CAPS/ELS spectrogram, in a supercorotating layer as identified from a leading magnetic field signature. Figure 2b, the same way as Figure 2a, shows the typical electron phase space density measured in this subregion, at 0721 UT. Subregion 3 (0733–0748 UT) is characterized by a bimodal feature composed of a low-energy beam (a few 100 eV) with a short (8 s) energy-time dispersion signature in addition to the energetic population which appears to narrow in energy, still in a supercorotating layer. Figure 2c displays the typical electron phase space density in this subregion, measured at 0744 UT.

3.1. Energetic Electron Population

[29] In the downward current time interval, the electron distributions systematically display evidence of a bump on tail between 1 and 10 keV (Figures 2a, 2b, and 2c) in the magnetic field antiparallel direction. Between 0640 UT and 0717 UT (Figures 2a and 2d), the electron population is observed to peak at energies lower than 10 keV, so almost all the population is measured by CAPS/ELS. The electrons appear to be highly field aligned, with fluxes 1000 times higher in the antiparallel direction compared to the perpendicular.

[30] Between 0717 UT and 0733 UT (Figures 2b and 2d), the peak gets broader in energy and pitch angle (field-aligned flux about 100 times higher than perpendicular flux) and the electron spectrum hardens, extending beyond the CAPS/ELS energy range. This is confirmed by measurements made by

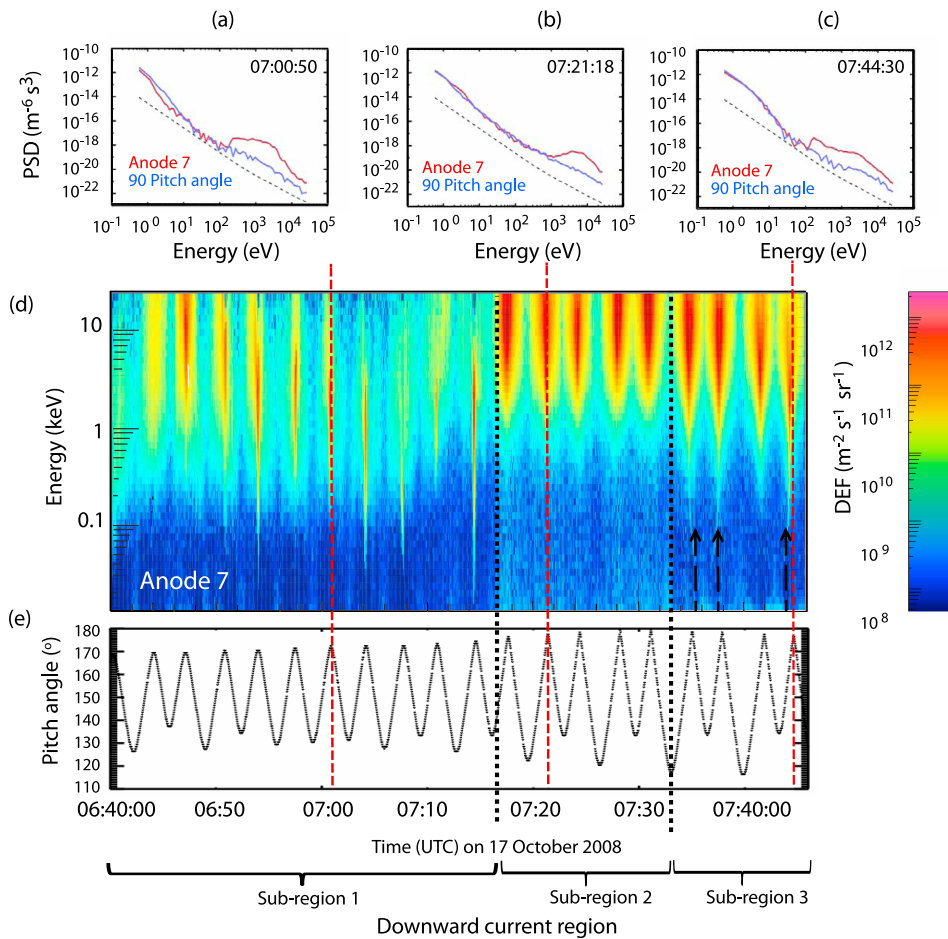


Figure 2. High-resolution CAPS/ELS electron measurements in the downward current region on 17 October 2008. (a, b and c) Three spectral cuts in phase space density, typical of each of the three identified downward current subregions. The flux in the antiparallel direction (covered by anode 7) and perpendicular direction are represented in red and blue, respectively, while the black dashed line defines the one-count level. (d) The full-resolution differential energy flux spectrogram as measured by anode 7. The spectrogram is separated in three parts (i.e., subregions) by two black vertical lines. The red dashed vertical lines point to Figures 2a, 2b, and 2c. The arrows point toward the dispersive low-energy beams after 0730 UT. (e) The pitch angle coverage of anode 7.

the MIMI/LEMMS instrument (Appendix B) which measures electrons from 20 keV to 10 MeV. The noise level observed in both CAPS ELS and IMS instruments also increases, indicative of significant fluxes of energetic electrons penetrating the CAPS instrument. Figure B1a shows a CAPS/ELS-MIMI/LEMMS composite energy spectrum averaged between 0717 and 0730 UT, from which we observe that the electrons from 1 keV to 200 keV belong very likely to the same population, forming a flat, unpeaked population in differential energy flux. These electron observations are very similar to the electron observations in the downward current region in the Earth's auroral region characterized by the following features: upward directed, narrow in pitch angle and displaying a broadband energy range [Marklund, 2009]. The step change in the character of the energetic electron flux within one actuator cycle at 0717 UT, is observed simultaneously as the enhancement of the low-frequency wave intensity.

[31] A careful analysis of the evolution of the spectrogram (Figure 2d) shows that the lower envelope of the broadband

electron population follows a V-shaped oscillation, with a deeper signature in subregion 1 (0640–0717 UT). This oscillation follows the pitch angle coverage of the anode 7 (pointing direction close to 180° at this time) as the actuator moves. In the present case, it shows that the energy is minimum in the more field-aligned direction and maximum at higher pitch angle. This distribution could either be the result of the combination of the acceleration through a field-aligned electric field and wave-particle interactions which would have diffused the energy out of the parallel direction. Or the distribution could be the result of the combination of transverse heating and parallel acceleration producing a “bowl-shaped” distribution previously seen in ion observations at Earth [Klumppar *et al.*, 1984; Horwitz, 1986].

3.2. Low-Energy Beams

[32] The end of subregion 2, at 0733 UT, coincides with the observation of a new feature, consisting of sporadic upward narrow beams appearing during short time intervals. These beams were not previously observed in Figure 1

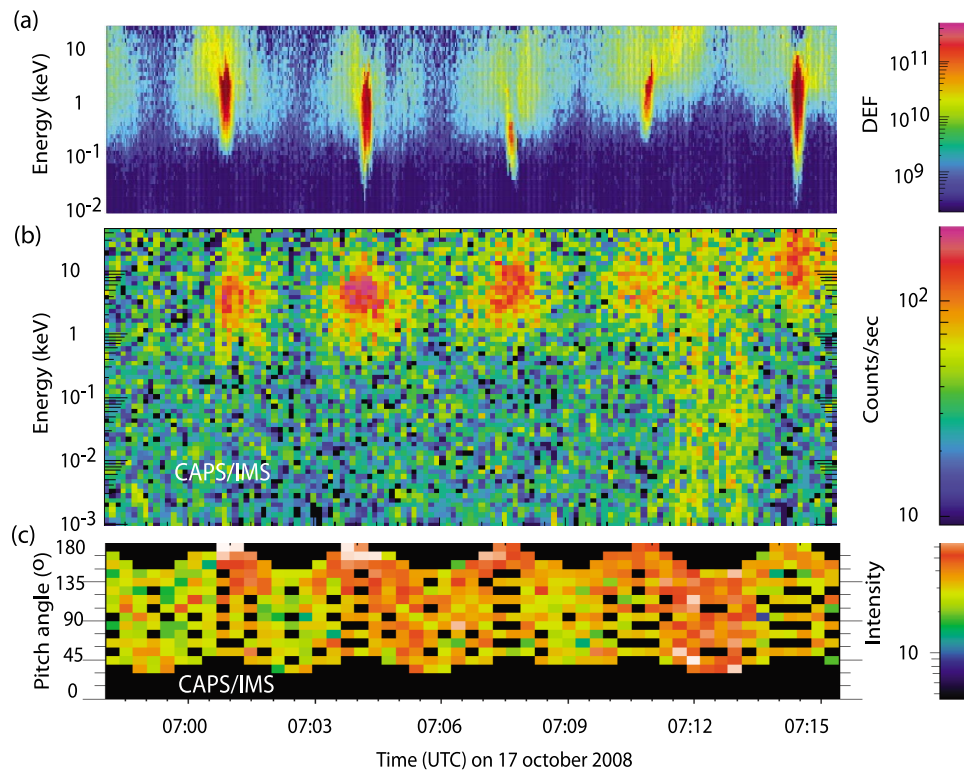


Figure 3. Large-scale ion and electron observations in the downward current region on 17 October 2008. (a and b) The CAPS/ELS high-resolution (2 s) and the CAPS/IMS energy-time spectrograms (in differential energy flux) in anode 7 (covering periodically the antiparallel pitch angle direction). (c) The pitch angle distribution of the 1–1.5 keV energy ion population in the same time interval.

because the 3 min resolution spectrogram aliases these short-timescale features. Figure 2c shows an energy spectrum of one of the beams, at 0744 UT. The beam appears as a sharp enhancement at about 200 eV in the upward direction, together with the broadband energetic electron population in the tail of the phase space distribution. In the energy-time spectrogram (Figure 2d), we observe several of these narrow electron beams, highlighted by the vertical dashed arrows. These display an energy-time dispersion, either increasing or decreasing, peaking at 180° pitch angle.

[33] The observed energy dispersion signature ranges from 100 eV to keV over a 12 s time interval. The dispersion cannot be due to time of flight effects along or across the magnetic field lines because these will only produce either strictly decreasing or increasing time dispersions. At Earth, a similar energy-time dispersive signature was identified by *Andersson et al.* [2002] in the downward current region and was interpreted as the result of the spacecraft obliquely crossing electrostatic equipotentials. But the simultaneous presence of two electron populations of different energies discards this possibility. An alternative explanation could be that the low-energy beams and the energetic electron population are linked: either the cooling of the broadband electron population may produce the lower-energy population, or the heating of the latter may generate the energetic population. In the magnetosphere, heating/cooling processes are mostly induced by WPI.

[34] In the Earth's auroral region, simultaneous observations of inverted-V electrons (a few keV) and low-energy

electrons displaying time-dispersive signatures were reported [*Kletzing and Hu*, 2001]. In order to explain these features, *Chen et al.* [2005] ran simulations of WPI between inverted-V electron populations and kinetic Alfvén waves (AW). They showed that such an interaction generates low-energy electrons with an energy-time dispersion through resonant deceleration. At Saturn, the Alfvén speed in downward current subregion 3 (0733–0748 UT) lies between 4×10^7 and 4×10^8 m s⁻¹, which is very close to the observed energetic electron population thermal velocity, allowing resonant interaction with possible existing AWs.

3.3. Ions

[35] Figure 3 displays the CAPS/ELS electron spectrogram (Figure 3a) and the CAPS/IMS ion spectrogram (Figure 3b) measured in anode 7, and the ion pitch angle distribution in the keV energy range (Figure 3c) in the 0658–0715 UT time interval, in the downward current region. The ion energy spectrogram shows evidence of enhanced upward ion fluxes and an analysis of the time-of-flight spectra (not shown) shows that these are composed of light ions. The ion pitch angle distribution peaks in the 180° direction with, however, a broader (more isotropic) pitch angle distribution compared to the electrons. The observed upward ions are consistent with the MIMI/CHEMS and MIMI/INCA energetic ion observations made during several high-latitude orbits in the downward current region, where *Mitchell et al.* [2009] identified energetic ion conics and ion beams associated with electron beams. While a downward directed ion population

is expected to be observed in a downward current region due to precipitation of magnetospheric ions, an upward ion population is detected. This feature has also been observed in the terrestrial magnetosphere and was tentatively explained by *Gorney et al.* [1985] in terms of ion heating due to WPI. In this interpretation ions are trapped close to the ionosphere below the electrostatic potential drop and continually heated perpendicular to the field by WPI. This process continues until the ions are sufficiently energetic that they can overcome the potential and escape from the ionosphere [Marklund, 2009]. This is referred to as the “pressure cooker effect.”

3.4. Acceleration Source

[36] At Earth, the acceleration source of electrons in the downward current region is a quasi-static electric field structure deriving from a potential drop at high latitudes [Marklund, 2009], and we will consider the same for Saturn. During the event examined here, the downward current region includes three subregions which display different large-scale trends (Figure 2), but all include the presence of strong upward electron beams, indicating the presence of a potential drop structure below the spacecraft.

[37] The determination of the exact value of the potential drop from the particle distribution is not straightforward because the observed particle energies are the results of the combination of different processes such as acceleration, thermalization, and wave-particle interactions. We are, however, not able to separate the different effects caused by these processes. The average energy, defined as the ratio of the energy flux and the total number flux, has been used to determine the average energy gained by the electrons in the downward current region [Carlson et al., 1998]. In the present study, we determined this quantity numerically, and we used it as an estimate of the potential drop, in the downward current region.

[38] Subregion 1 (0640–0717 UT) is consistent with the presence of a potential drop structure below the spacecraft which decreases slowly with time, which might be a temporal change in the acceleration region or due to the spacecraft crossing a spatially varying acceleration region. We estimate an electron average energy of a few keV from the CAPS/ELS data and of about 10 keV from the whole CAPS/ELS-MIMI/LEMMS spectra. The potential value obtained using only CAPS/ELS data is very likely underestimated because the electron spectra extends beyond the upper limit of the CAPS/ELS detector. Therefore, we infer a potential drop between the magnetosphere and ionosphere of 10 kV, corresponding to a downward electric field, in subregion 1. Subregion 2 (0717–0733 UT) and subregion 3 (0733–0744 UT) show a rather stable large-scale energy distribution implying a constant potential drop below the spacecraft. We estimate an average energy of 50 keV from the composite spectra, which implies a potential drop estimation of 50 kV between the magnetosphere and ionosphere in subregions 2 and 3.

[39] The important step change at 0717 UT of the energy and intensity of the energetic electrons indicates an impulsive modification of the magnetosphere-ionosphere coupling the accelerating structure (potential drop). *Sagdeev and Galeev* [1966] argued that the interaction between electric field turbulence and current carriers introduces an effective (anomalous) resistivity along the magnetic field line. In the presence of a field-aligned current, the resistivity could

produce parallel electric fields which may accelerate the electrons and create the observed accelerated beams.

3.5. Wave-Particle Interactions

[40] The electron populations accelerated from the ionosphere through a potential drop are not monoenergetic and not completely field aligned, displaying a nonnegligible perpendicular component. Moreover, an enhancement of the low-frequency electric waves is observed below 4000 Hz in the 0715 and 0745 UT time interval (Figure 1a), coincident with the intensification/energization of electron beams and accelerating structures in subregions 2 and 3. The presence itself of the low-frequency waves in a region where the electron phase space density displays a nonnegligible positive slope $\partial f/\partial v_{\parallel}$ raises the question of wave generation via plasma instabilities which may have a role in scattering the electrons in energy and pitch angle. At Earth, electron-driven and current-driven instabilities were identified as the source of wave generation. Current-driven instabilities may generate low-frequency large-amplitude turbulent electric fields as observed on terrestrial auroral field lines [Gurnett and Frank, 1977]. Nonthermal populations displaying positive $\partial f/\partial v_{\parallel}$ or $\partial f/\partial v_{\perp}$ have been identified as a free-energy source for several instabilities leading to wave production such as whistler mode emissions (i.e., auroral hiss) via the beam plasma instability [Maggs, 1976], or AKR via the cyclotron maser instability [Wu and Lee, 1979]. As the instability develops and the waves grow, the electrons are expected to scatter in energy. According to this, the energetic broadband electron population observed from 1 keV to 200 keV in subregion 2 may result from (1) the acceleration through a 200 kV potential drop and (2) the cooling to 1 keV by WPI. In addition to the whistler mode, the broadband extremely low frequency waves (BBELF) and electron solitary waves (ESW) identified in the Earth’s downward current region are also good candidates to thermalize and broaden the electron energy distribution. The interaction of the turbulent waves with the current carriers could also introduce a resistivity along the magnetic field lines as discussed in section 3.4. As discussed earlier, Alfvén waves may play a role in the production of the low-energy electron time dispersive electron beams. We therefore examined the plasma wave data to identify their presence, but the instrument is not sufficiently sensitive at these low frequencies. The identification of Alfvén waves will probably need further magnetic data analysis.

[41] In the future, calculations of the energy and pitch angle diffusion coefficients [Glauert and Horne, 2005] and the solution of the full Fokker-Planck equation will be necessary to determine the exact role of wave-particle interactions.

4. Observations in the Upward Current Regions and SKR Source Region

4.1. Electron Populations

[42] From the magnetometer data presented in Figure 1g, two upward current regions can be identified (highlighted in red): a first upward current layer on closed field lines typical of the predusk high-latitude magnetosphere [Talboys et al., 2009b; Bunce et al., 2010] in the 0620–0640 UT time interval, and a second (unusual) upward current layer coincident with the SKR source region, in the 0750–0900 UT time interval. In both cases there are no obvious strong asymmetries in

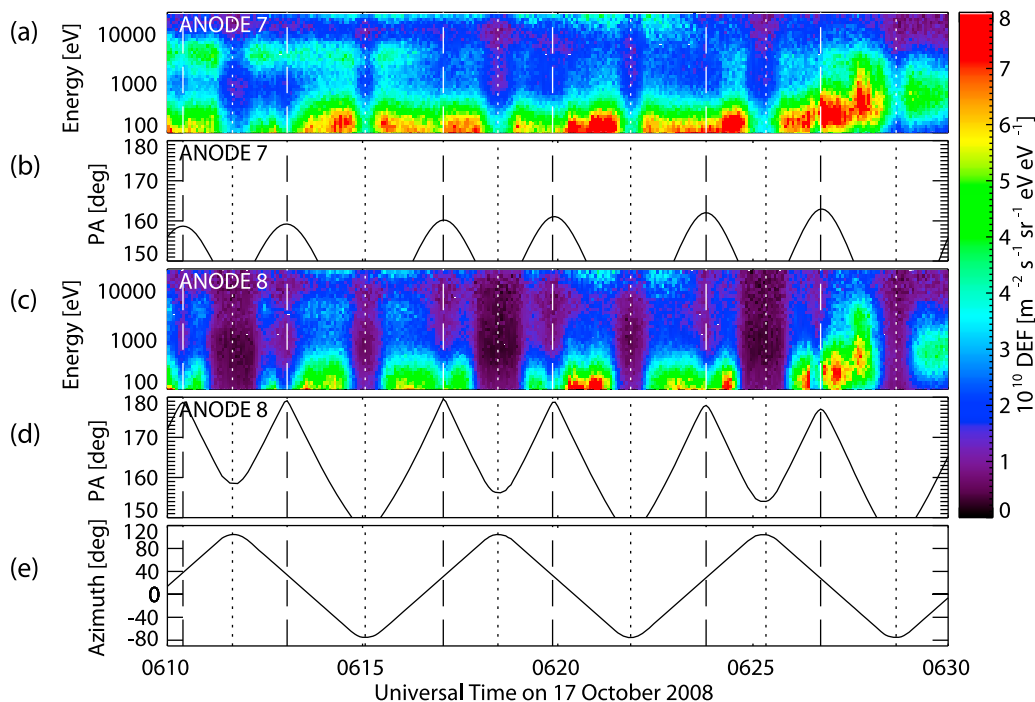


Figure 4. Loss cone distribution in the upward current region on 17 October 2008. (a and c) CAPS/ELS electron spectrograms in anodes 7 and 8 in the 0610–0630 UT time interval. (b and d) Pitch angle coverage of the center of the anodes 7 and 8. (e) Azimuthal position of the actuator. The vertical dotted lines highlight the times the actuator goes to its extreme positions. The vertical dashed lines denote the times when the anode 8 look direction is aligned with the 180° pitch angle direction.

the electron flux to indicate larger downgoing fluxes in order to carry the field-aligned currents suggested by the magnetometer data.

[43] From Figures 1b, 1c, and 1d, we observe that in the 0630–0640 UT interval, the flux of both thermal and supra-thermal populations drops by a factor of 100 to near background levels. In the poleward upward current region, the upward electron fluxes are still present in the 0748–0800 UT interval but with a decreasing intensity. Following this, the flux of warm (0.1–1 keV) electrons approaches the noise level, and the high-energy (keV) electron flux is 100 times smaller than in the previous region and has a much broader pitch angle distribution.

4.1.1. Loss Cone

[44] Although there is no strong evidence of a high flux of precipitating electrons in the upward current regions due to the lack of sampling, the observation of an enhanced loss cone in the antiparallel direction could present evidence for the existence of the observed upward current. Figure 4 presents time-energy electron spectrograms from anodes 7 and 8 of CAPS/ELS, the pitch angles of the center of these anodes, and the actuator angle of the CAPS instrument. The large depletions in flux (of a factor of ≈ 3 –4), particularly observed in anode 8 for example around 0615 and 0618 UT, and to a lesser extent at the same times in anode 7 are due to obscuration of the CAPS/ELS field of view by other instruments and various parts of the spacecraft [Young *et al.*, 2004]. One can see that these decreases in flux occur around extremes in the actuator angle of CAPS/ELS (vertical dotted lines). Smaller reductions in flux (of a factor of ≈ 1.5) are observed as the pitch angle of anode 8 approaches 180°,

denoted by the vertical dashed lines. These reductions in flux are not mirrored in anode 7. We argue that these reductions in flux are loss cones. A simple estimate of the width of these loss cones gives a width around 11° at the location of Cassini. A second example is presented in Figure 5 from the second upward current region. In the first part of this region, the high upward electron fluxes having been accelerated in the previous region are still observed. However, unlike in the downward current region a cutoff appears in the apex of the V-shaped signature, when the anode 7 look direction approaches 180°. The largest depletion in flux (of a factor of ≈ 2) is observed in this anode and is not reflected in anode 8, which gives a slightly smaller width estimation of 9°, whereas the standard atmospheric loss cone should be around 5° with an ionospheric height of 1000 km [Gérard *et al.*, 2009]. This difference may rise from the combination of (1) instrumental effects (e.g., aperture size) which can affect the profile of the flux as a function of the orientation of the sensors (the anode size (20° × 5°) and acceptance cannot resolve the loss cone, such that the depletions in flux in the loss cone may be underestimated) and (2) the presence of a potential drop below the spacecraft which may enhance the number of precipitating electrons into the ionosphere.

[45] At this stage, it is not possible to separate the instrumental effects and robustly identify the presence of a broadened loss cone which supports the downward acceleration of electrons below the spacecraft. However, as reported in section 4.2, the presence of upward accelerated ion beams (indicative of an accelerating potential), as observed in the second upward current region support the identification of field-aligned currents in the magnetometer data.

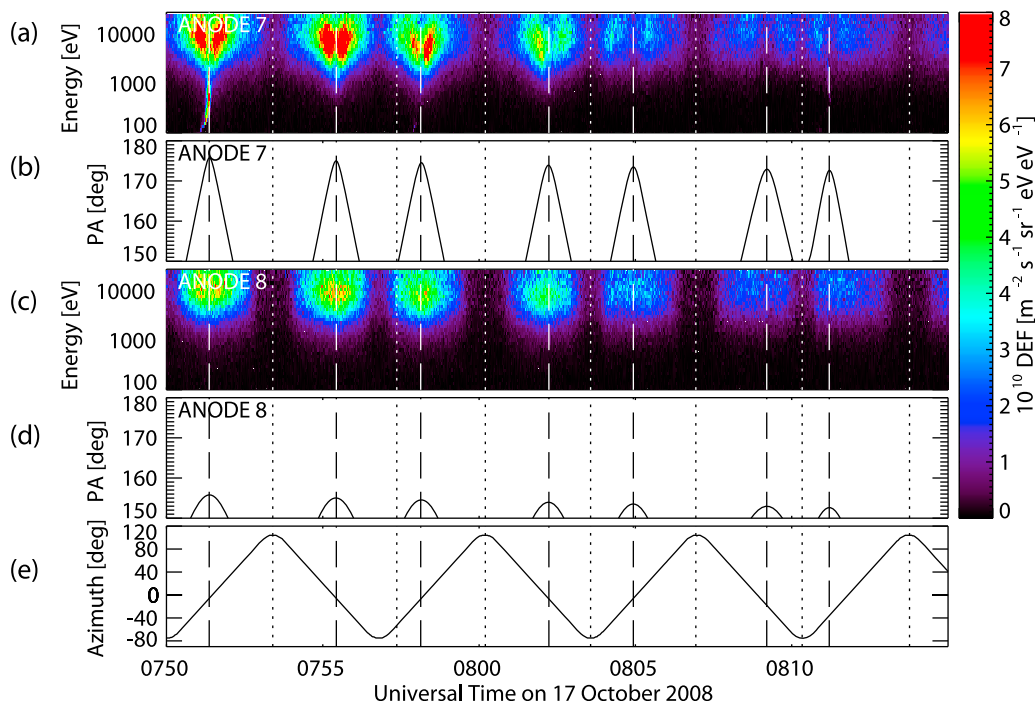


Figure 5. Same as Figure 3 but in the second upward current region 0750–0815 UT.

4.1.2. Shell Distribution

[46] Although the average electron fluxes in the second upward current region (0748–0900 UT) are very low compared to those observed in the downward current region (0640–0748 UT), we observed some evidence of net downward electron fluxes in the few keV energy range (for example at 0820 UT and 0840 UT in Figure 1e). From 0840 to 0855 UT, *Lamy et al.* [2010] identified unambiguously three SKR source crossings (orange vertical lines in Figure 1) according to the criteria used at Earth: (1) an enhanced amplitude of the low-frequency envelope and (2) a cutoff frequency close to or strictly below the electron cyclotron frequency.

[47] Figure 6a displays the three-dimensional electron phase space density as a function of v_{\parallel}/c and v_{\perp}/c at the times the spacecraft crossed two of the three SKR sources [*Lamy et al.*, 2010] (at 0840 UT and 0855 UT). The third source (0852 UT) has not been displayed here because the downward pitch angle directions were not properly covered. These distributions have not been corrected for noise. Figure 6b displays the phase space density in the downward direction (averaged over the 0–90° pitch angle direction) as a function of energy. Figures 6c and 6d show the energy-time electron spectrogram measured by anode 2 and its pitch angle coverage. From Figures 6c and 6d, we observe that the electron flux is lightly enhanced (factor of about 3–4) when the anode direction approaches the low pitch angles (highlighted by the red vertical lines). During source crossing, the averaged downward flux (from 0 to 90°) appears systematically higher than the upward flux (from 90 to 180°).

[48] From Figure 6b the electron distributions show some evidence of a bump-on-tail feature peaking between 3 and 9 keV. However, it is important to note that although the phase space density near the peak is 100 times higher than the

noise level, before the peak it is close to the background level and has a signal-to-noise ratio of around 2. The implication of such a low signal-to-noise is that the bump on tail either (1) could be much stronger than is apparent in the observations providing a large $\partial f/\partial v_{\perp} > 0$ nonthermal feature or (2) could actually be consistent with a more-or-less isotropic distribution with $\partial f/\partial v_{\perp} < 0$ which is stable to the CMI.

[49] To investigate further the nature of these electron distributions we modeled the observed distribution with (1) a Maxwellian model and (2) a Maxwellian multiplied by a power law $(v/a)^k$, where a is the thermal energy and k a proxy for the positive slope, which allows us to take into account the apparent bump (positive slope). The latter distribution is known as the Doris-Guest-Harris (DGH) distribution [*Dory et al.*, 1965] and was introduced to model such nonthermal features. The results are presented in Figure 6b, where the Maxwellian and the DGH models are superimposed in blue and red, respectively. Although we have not weighted the fit to account for the poor signal to noise, the DGH model can be seen to qualitatively reproduce the observed distribution, particularly the high-energy tail of the distribution.

[50] The measured distributions are suggestive of a “shell” distribution deriving from (1) the acceleration of electrons downward along magnetic field lines, (2) conservation of the first invariant μ , and (3) conservation of kinetic energy. Such a shell distribution requires an acceleration region above the spacecraft, i.e., between the spacecraft and the magnetosphere. These nonthermal distributions have been detected in the terrestrial magnetosphere and can generate AKR through the CMI [e.g., *Ergun et al.*, 2000]. The poor signal in the measured saturnian distributions may be related to modification of the shell distribution by WPI. SKR growth rates calculated from these DGH fits have been presented by

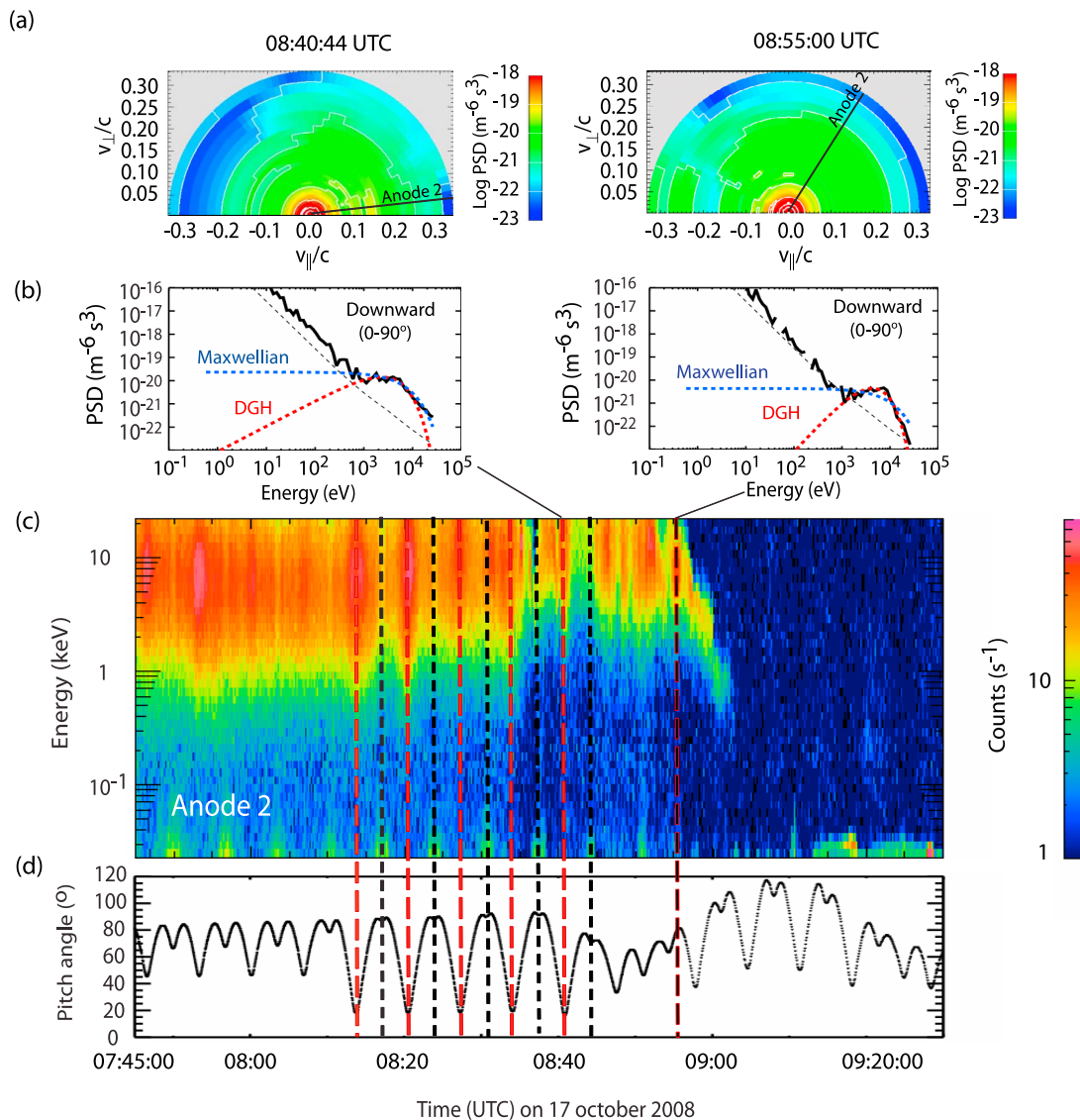


Figure 6. Downward electron flux and shell-like distribution close and within the SKR source region on 17 October 2008. (a) Three-dimensional phase space density in two of the three SKR source crossing regions identified by *Lamy et al.* [2010] at 0840 UT (Figure 6c) and 0855 UT. The electron distribution has been interpolated between the pitch angle sectors to display a full distribution function in those images. (b) Average downward electron phase space density with the adjusted Maxwellian distribution model (in blue) and the DGH model (in red) in function of energy. (c) Energy spectrogram measured by anode 2. (d) Pitch angle coverage of anode 2.

Mutel et al. [2010] and show significant SKR growth, although the effects of low signal to noise on the DGH fits and consequently on the growth rates have not been explored.

4.1.3. Upward Electron Beams

[51] In addition to the previous downgoing electron features, sporadic upward electron beam features are observed in the 100 eV energy range, similar to those observed in the downward current region (8 events identified from the present analysis, not shown here). The presence of these upward directed electrons is unexpected in the large upward current region. However, a careful analysis of the azimuthal component of the high-resolution magnetic field (1 s) during the occurrence of those beams shows that very fine downward

current structures, with a duration of around 8 s, are embedded in the large upward current region. Figure 7 shows an example of such fine structure from the 0835 to 0840 UT time interval. Figure 7a shows the azimuthal magnetic field component; Figures 7b and 7c display the electron differential energy flux in anode 6 and the anode pitch angle coverage, respectively. The beams are observed to be highly aligned along the magnetic field, with pitch angles above 170° . Each low-energy beam seems to be correlated with a very fine downward current structure, highlighted by the red vertical lines. The origin of these upward electron beams in the large upward current region is not clear but implies these electrons are accelerated by small downward electric field structures

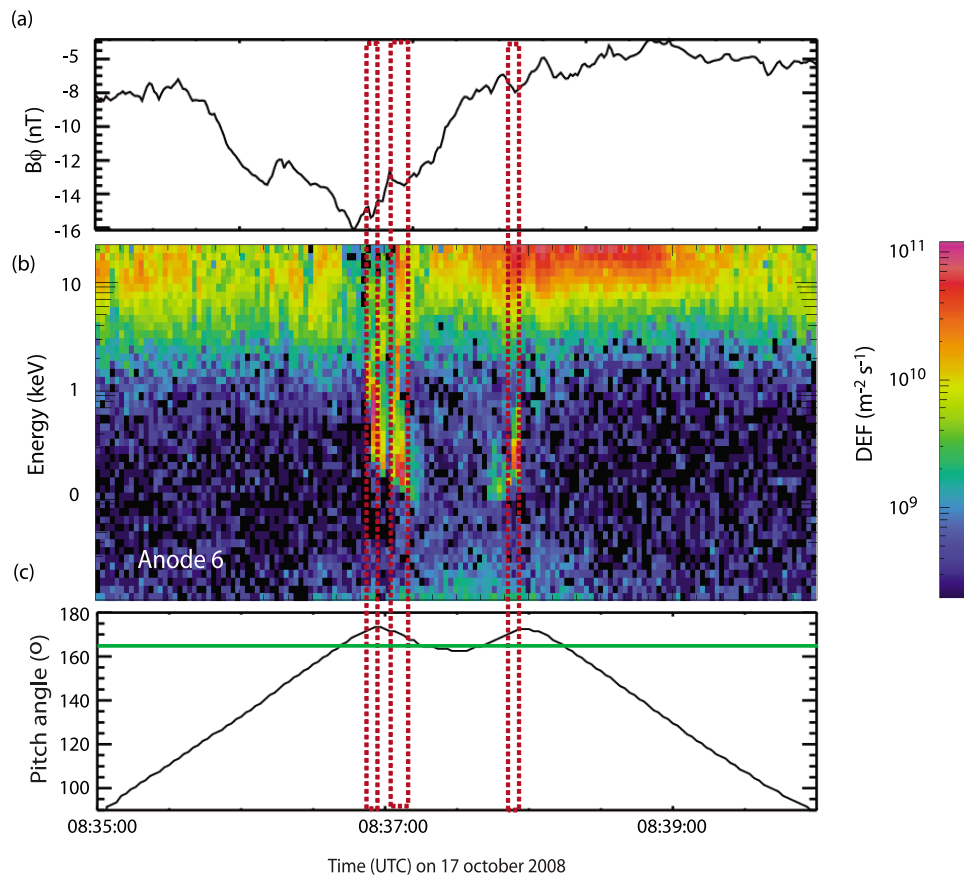


Figure 7. Small-scale downward current signatures embedded in the large-scale upward current region and associated upgoing electron beams on 17 October 2008. (a) Azimuthal magnetic component. (b) CAPS/ELS spectrogram measured by anode 6. (c) Pitch angle coverage of anode 6. The red dashed vertical boxes highlight the correlated magnetic field structures and the simultaneous upward electron beams in the 0835–0840 UT time interval. The horizontal green line in Figure 7c shows the higher pitch angle limit of the observed upward electron beams.

embedded in the large-scale upward current region. In auroral regions at the Earth, *Hultqvist et al.* [1988] observed coincident upward flow of ions and electrons. *Hultqvist* [1988] demonstrated that these observations can arise from the combined effect of a DC electric field and a fluctuating electric field. While the ions are in average only accelerated by the DC component, the fluctuating electric field appears as quasi-static for the electrons and accelerates the electrons in the upward direction when it is pointing downward, allowing the electrons to leave the DC electric field acceleration region before the electric field switches direction. In the Jovian magnetosphere, *Mauk and Saur* [2007] found that the structure of currents at lower latitudes, which map to the auroral region, is composed of intermixed magnetic field lines carrying upward and downward currents.

4.2. Ions

[52] Although no significant ion fluxes are observed in the first upward current region (0620–0640 UT), strong ion flux enhancements were measured in the second upward current region (0748–0900 UT).

[53] Figure 8 displays the CAPS/ELS electron and CAPS/IMS ion spectrograms (Figures 8a and 8b), and the ion

pitch angle distribution at 1 keV (Figure 8c), during the 0815–0900 UT time interval. We first observe that the ion energy flux in this region is about 10 times higher than in the downward current region. The ion pitch angle distribution shows that the flux is mainly concentrated around the upward direction (180° pitch angle), consistent with the upward current direction. Two distinct ion populations can be found: a first population ranging from 1 keV to 10 keV which decreases in energy to a few hundred eV in the 0800–0900 UT time interval, and a second population (circled in red), highly field-aligned and very energetic (above 10 keV). This latter population appears at exactly the same timing as the beams identified by *Mitchell et al.* [2009, Figure 5] from MIMI/INCA observations at 0837 UT and 0855 UT and may be the low-energy component of these beams. Analysis of the composition of these ion beams showed the ions were mainly H^+ and H_3^+ (F. Cray, private communication, 2010), consistent with an accelerated ionospheric plasma source.

4.3. Acceleration Source

[54] In the upward current region we observed three different electron distributions that probably arose from different acceleration processes.

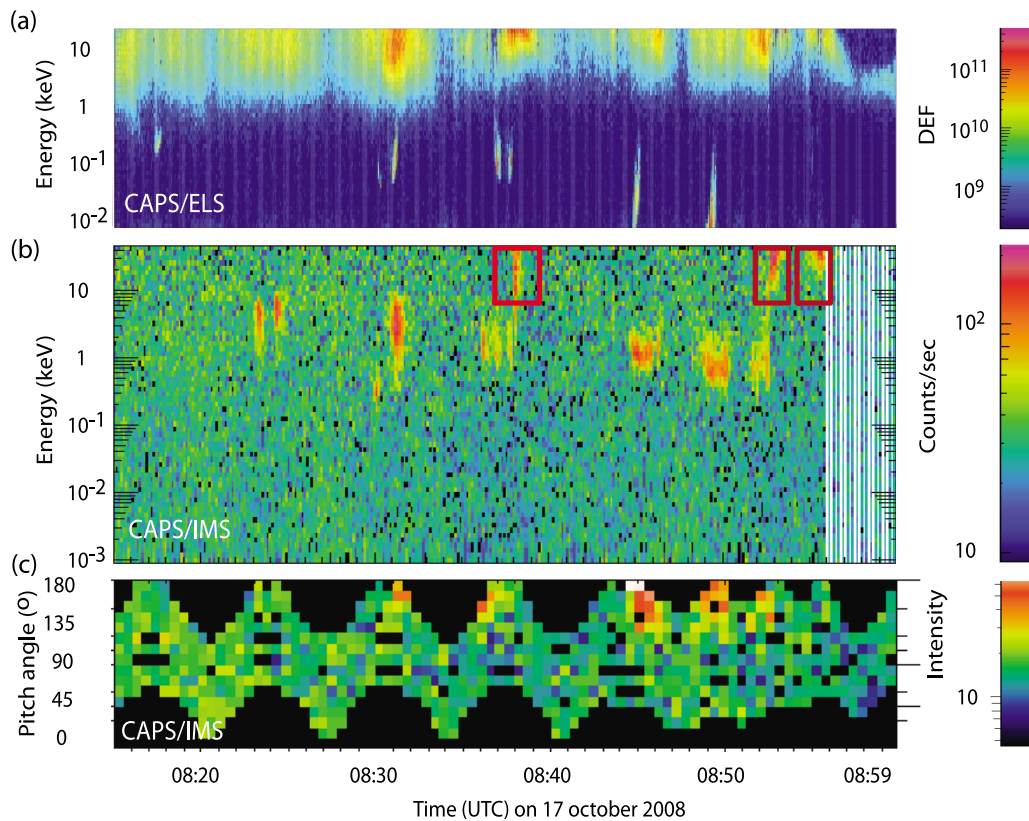


Figure 8. Large-scale ion and electron observations in the upward current region on 17 October 2008. (a and b) The CAPS/ELS high-resolution (2 s) and the CAPS/IMS energy-time spectrograms (in differential energy flux) in anode 7 (180° pitch angle coverage). (c) The pitch angle distribution of the keV energy ion population in the same time interval at 1 keV. The flux enhancements enhanced by the red boxes are the low-energy counterpart of the very energetic peaks identified by *Mitchell et al.* [2009, Figure 5] from the ion neutral camera of MIMI.

[55] First, the possible existence of a broadened loss cone distribution implies the existence of an acceleration region below the spacecraft. The presence of upward accelerated ions in the same region confirms this statement. The average energy of the ion beams is about 10 keV at 0815 UT to 1 keV at 0900 UT, which gives an estimation of the potential drop between the ionosphere and the magnetosphere of 1 kV to 10 kV in the poleward upward current region (under the assumption the ion energy measured at the spacecraft is about the same as just above the potential drop). These estimated potentials are consistent with those presented by *Bunce et al.* [2008] from magnetic field and plasma electron data during a crossing of field lines connected to the main auroral emission.

[56] Second, the possible presence of a shell-like distribution in the poleward upward current region would imply the existence of an acceleration region above the spacecraft. The acceleration could originate from a field-aligned potential drop or an injection event in the magnetodisc with conservation of the second invariant leading to an increase in the parallel velocity of the electrons. From the observed intensification of the integrated SKR power and its extension as low as 10 kHz, *Bunce et al.* [2010] reported a possible magnetospheric compression by the solar wind which may have triggered hot plasma injection into the magnetosphere.

[57] Third, the presence of upward warm electron beams may imply the existence of small downward potential drops embedded in the large-scale upward current region.

[58] Figure 9 shows a summary of the inferred potential drop structures in both the downward current region (in blue) and upward current region (in red for the potential derived from the warm ion energy peaks, in black for the potential derived from the very energetic peaks).

4.4. Cold Electron Density

[59] It is particularly well known that the AKR source region is depleted of cold plasma (50–1000 eV) by a factor of 5–10 with respect to the surrounding regions [*Louarn et al.*, 1990; *Roux et al.*, 1993]. Figure 1f shows the plasma density in different energy ranges, throughout the period. One can immediately see that no such plasma density cavity is observed in the SKR source region [*Lamy et al.*, 2010], and indeed, the cold plasma density is relatively low throughout the pass, consistent with many high-latitude passes of Cassini through Saturn's high-latitude magnetosphere. It is, however, possible that very cold plasma density cavities do exist, close to or below the energy range of the CAPS/ELS instrument (see discussion in Appendix C). However, the existence of cold very dense populations would have a charging effect which is not observed.

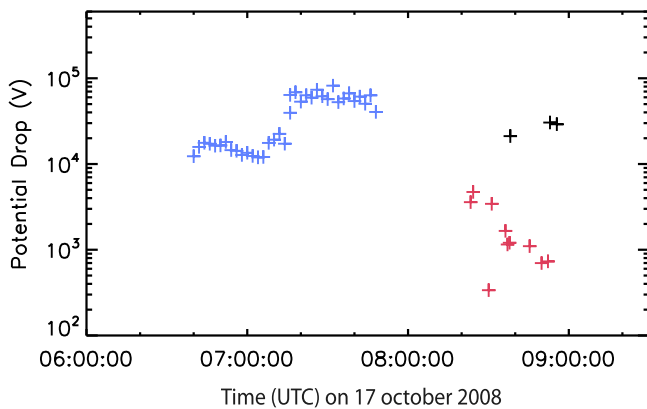


Figure 9. Potential drop (in volts) parallel to the magnetic field on 17 October 2008. In the downward current region, the potential value was derived from the electron average energy determined from the CAPS/ELS and MIMI/LEMMS composite data. In the upward current region, the potential value was derived from the warm ion energy peaks (within the 1–10 keV energy range, in red) and from the very energetic peaks (above 10 keV, in black) identified in the CAPS/IMS spectrogram (Figure 8).

4.5. Wave-Particle Interaction and Free-Energy Source for SKR

[60] Two types of emissions are observed in the upward current region.

[61] The first type consists of low-frequency waves below 4000 Hz as observed in the downward current region and observed from 0800 UT to 0945 UT. *Kopf et al.* [2010] identified those as terrestrial-like broadband electrostatic noise and auroral hiss emissions. These emissions have previously been observed at the Earth in upward current regions [Gurnett and Frank, 1977; Carlson et al., 1998]. *Kopf et al.* [2010] computed growth rates and deduced that the positive slope $\partial f/\partial v_{\parallel}$ of the narrow electron beam distribution observed at 0835 UT was sufficient to drive the observed whistler mode auroral hiss emissions, as in the downward current region.

[62] The second type consists of SKR emission in the 10^4 – 10^6 Hz frequency range, whose properties have been shown to be consistent with generation by the CMI mechanism. *Lamy et al.* [2010] observed that the relativistic shift of the SKR cutoff frequency below the electron cyclotron frequency f_{ce} is consistent with the observed energetic electron populations (6–9 keV) at times the spacecraft crossed the sources. Contrary to the case of the Earth, the whole region surrounding the SKR source appears to be devoid of cold plasma without a density cavity.

[63] Three nonthermal electron distributions were observed in the surrounding time intervals: low-energy beams, an enhanced loss cone, and a shell-like distribution. First, the low-energy beam seems to be a poor candidate to drive the cyclotron maser instability because it does not display the positive $\partial f/\partial v_{\perp}$ slope required to drive the CMI, and the distribution only covers a small part of the resonant circle. Second, the loss cone is observed at the beginning of the second (poleward) upward current region but is no longer

visible inside the SKR source region as the electron intensities become very low. So no obvious loss cone is observed at the precise SKR source location. Furthermore, a loss cone distribution would drive a CMI oblique emission while a quasi-perpendicular emission is actually observed [Lamy et al., 2010, 2011]. Third, the electron distribution tail within SKR source location has a smoothed/plateaued bump-on-tail shape which may have resulted from the relaxation of an initial important bump-on-tail distribution displaying a positive $\partial f/\partial v_{\perp}$ slope. Such plateaued distributions have been previously observed during AKR source crossings by *Winglee and Pritchett* [1986] and *Delory et al.* [1998] and can be explained by diffusion times which are shorter than the time resolution of the analyzer.

[64] *Mutel et al.* [2010] reported that the shell distribution is able to drive the CMI for several times in the 0843–0854 UT time interval. The shell distribution is a good candidate, because its temperature is sufficient to create a relativistic shift of the SKR frequency below the electron cyclotron frequency, the center of the resonant circle is such $v_{\parallel} = 0$ and the SKR emission is observed to be quasi-perpendicular to the magnetic field at the source [Lamy et al., 2010]. The shell distribution fulfills the necessary condition and may be considered as the best candidate to drive the SKR. At Earth, *Ergun et al.* [2000] showed that the AKR growth rate for a shell distribution is much higher than for a loss cone distribution. Future crossings of the SKR source region will hopefully enable us to confirm the role of shell distributions as the main driver of SKR emission.

5. Summary and Conclusion

[65] On 17 October 2008, Cassini observed an unusual magnetospheric event in Saturn’s south hemispheric high-latitude region, characterized by (1) the presence of intense flux of high-energy electrons, (2) a strong enhancement of the wave activity with an intense SKR signal close and below f_{ce} indicating an SKR source crossing, and (3) very intense field-aligned currents extending to unusually high latitudes.

[66] Figure 10 shows a summary of the observations and Cassini spacecraft trajectory through the regions identified and our interpretation of the event. Cassini first crossed an upward (in red) current region between 0620 and 0640 UT, then crossed a downward (in blue) current region between 0717 and 0748 UT, and a second upward current region between 0748 and 0900 UT, where the SKR source was identified. The associated electron and ion observations, as well as the waves and the acceleration regions (V_{\parallel}) are indicated.

[67] From our multi-instrument analysis we reported the following.

[68] 1. In the downward current region, there is evidence of upward electron beams indicating the presence of a parallel electric field below the spacecraft which accelerates the electrons from the ionosphere to the magnetosphere. In the upward current regions, corresponding to the usual auroral magnetic field lines at Earth, we observed loss cone distributions, which may be broadened by an upward electric field accelerating the ions from the ionosphere toward the magnetosphere, below the spacecraft. A shell-like distribution is also observed in the upward current region. By analogy to the Earth auroral observations in the downward and

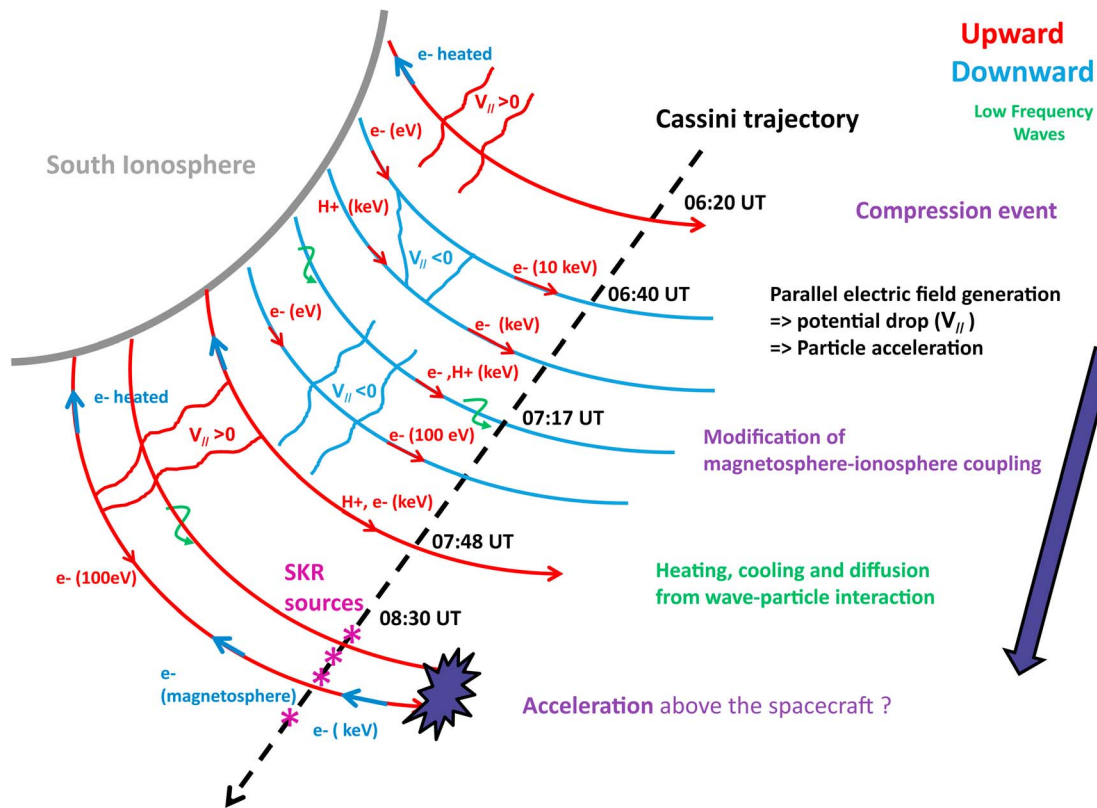


Figure 10. Sketch of the apparent spacecraft trajectory through the acceleration regions in Saturn's southern magnetosphere on 17 October 2008. The magnetic field lines carrying the upward current and the electron and ion flows are red. The magnetic field lines carrying the downward current and the electron flow are blue. The potential drops (V_{\parallel}) are indicated by two (equipotential) lines perpendicular to the magnetic field lines.

upward current regions, these observations present very similar characteristics.

[69] 2. The ion distribution properties appear to be similar to those identified at Earth. In the downward current region, an upward ion beam population is observed, consistent with the results of *Mitchell et al.* [2009]. At Earth, those observations were explained in terms of perpendicular ion heating by waves [*André and Chang*, 1994]. The energetic and directional properties of the particle distributions and the presence of intense low-frequency waves indicate the importance of the wave-particle interactions. A further study will be dedicated to the credibility of this scenario by a deeper analysis of the role of the low-frequency waves. Upward directed ion beams are observed in the upward current region and support the idea of the presence of a potential drop of a few kV accelerating the magnetospheric electrons into the ionosphere.

[70] 3. The energy range of the electron populations observed at high latitude in Saturn's magnetosphere is at least 1 order of magnitude higher than the usual magnetospheric populations. The energy is also much higher than the energies measured at Earth. *Mitchell et al.* [2009] have presented an argument for this elevated energy in terms of differences in magnetospheric scale between Earth and Saturn.

[71] 4. We find evidence of nonthermal electron distributions with positive gradients in their velocity distributions. Upward beams have been found to drive whistler mode

emission as observed at low frequencies in the downward current region. Evidence for a shell distribution has been used to estimate the growth rates for the cyclotron maser instability and the results show that these shell distributions could be the source for SKR emissions in the upward current region.

[72] 5. The properties of the electron distributions within the SKR source region showed that, unlike the AKR source region there is no density cavity, the plasma density around the source region being sufficiently low. But, like the terrestrial case, (1) the electron distribution in the source region is shell-like, (2) upward ion beams of several keV are observed, and (3) the magnetic data are consistent with the presence of upward field-aligned currents.

[73] 6. Cassini's crossing through the SKR source region and its vicinity is unique. The data presented in this paper display unusual features, even where similar orbits covered the same latitudes and radial distances. The reason may be an unusual dynamical event like a magnetospheric compression deriving from peculiar activity in the magnetospheric tail triggered by internal (centrifugal) or external (solar wind) forces and implying changes in the magnetosphere-ionosphere coupling. The consequences are (1) the generation of intense parallel electric field accelerating particles downward and upward along magnetic field lines, (2) the generation of highly unstable particle distributions, (3) the generation of intense

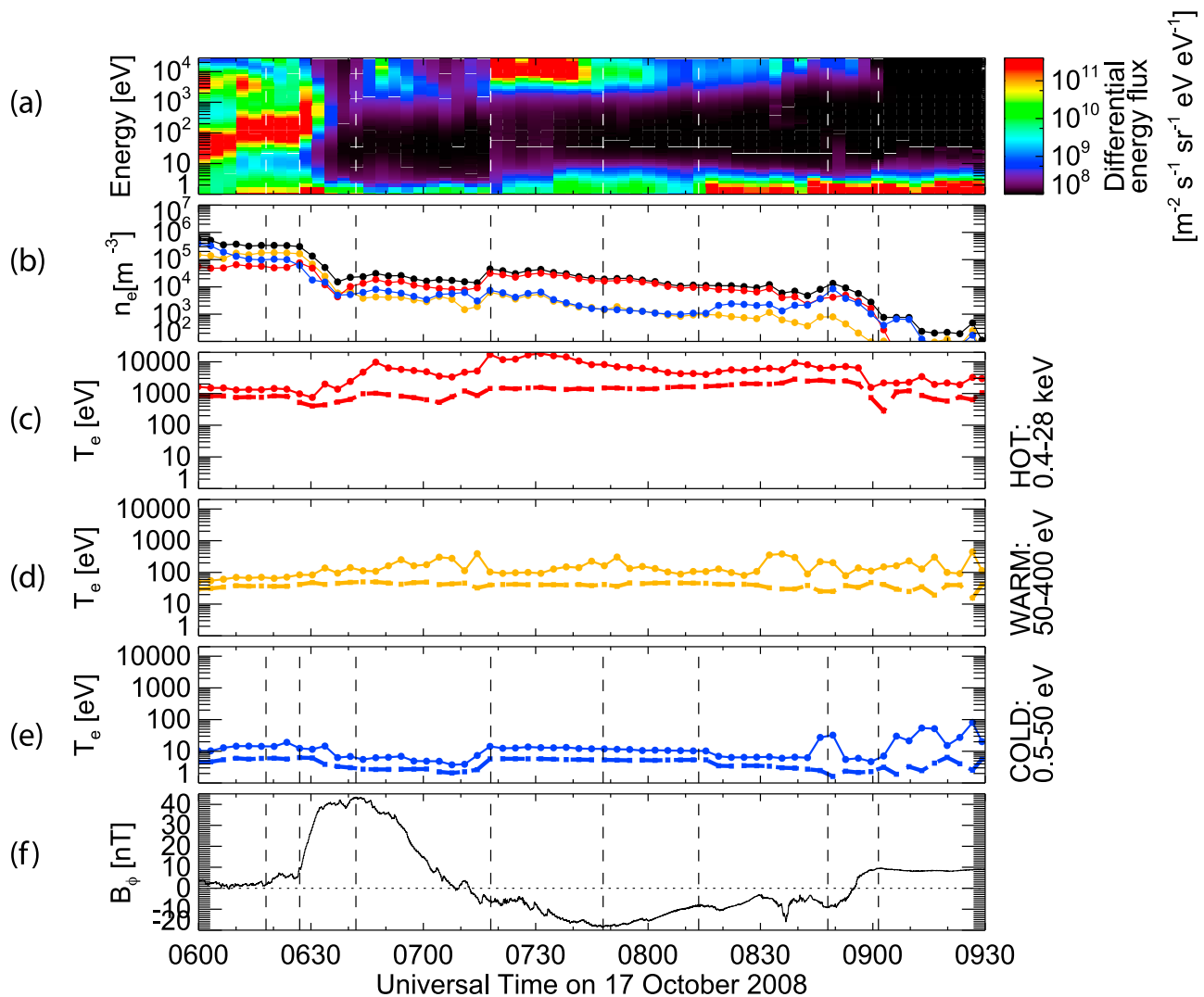


Figure A1. Electron density and temperature on 17 October 2008. (a) The omnidirectional CAPS/ELS energy-time spectrogram. (b) The density of the cold (0–50 eV, in blue), warm (50–400 eV, in yellow), and hot (400–28,000 eV, in red) electron populations and the total electron density (0–28,000 eV, black). (c, d, and e) The parallel (circles) and perpendicular (squares) temperatures of the hot, the warm, and the cold electron populations, respectively. (f) The azimuthal component of the magnetic field.

waves via electron-driven (or current-driven) instabilities, and (4) the generation of wave-particle interactions modifying the particle distributions.

[74] Future observations during the high inclination phase at the end of the Cassini solstice mission will provide another opportunity to explore these distributions and test the findings discussed in this paper.

Appendix A: Electron Moments

[75] Figure A1 shows electron moments calculated from the observed CAPS/ELS energy and pitch angle distributions. Figure A1a presents the energy-time spectrogram of the electron flux, Figure A1b the electron number density where black is the total density, red is the hot electron density (400–28,000 eV), orange is the warm electron density (50–400 eV), and blue is the cold (0.5–50 eV). Figures A1c–A1e show the

hot, warm, and cold electron parallel (circles) and perpendicular (squares) temperatures. Figure A1f shows the azimuthal component of the magnetic field. The electron moments were obtained from a direct integration over the observed distribution, assuming that the distribution is gyrotropic in the spacecraft frame. Gaps in the distribution (produced by poor pitch angle coverage) were filled by assuming that the distribution was symmetric about a pitch angle of 90° . At the start of the interval the total electron density was dominated by cold electrons with a rapid transition to warm electrons, consistent with the electron energy spectrum. After 0640 UT in the downward current region the electron density is completely dominated by hot electrons which is maintained until close to the end of the interval where narrow upward electron beams are observed in the upward current region. Generally the electrons have a $T_{\parallel}/T_{\perp} > 1$ temperature anisotropy, although the small anisotropies generally observed in the cold and warm electrons are probably close to the noise level

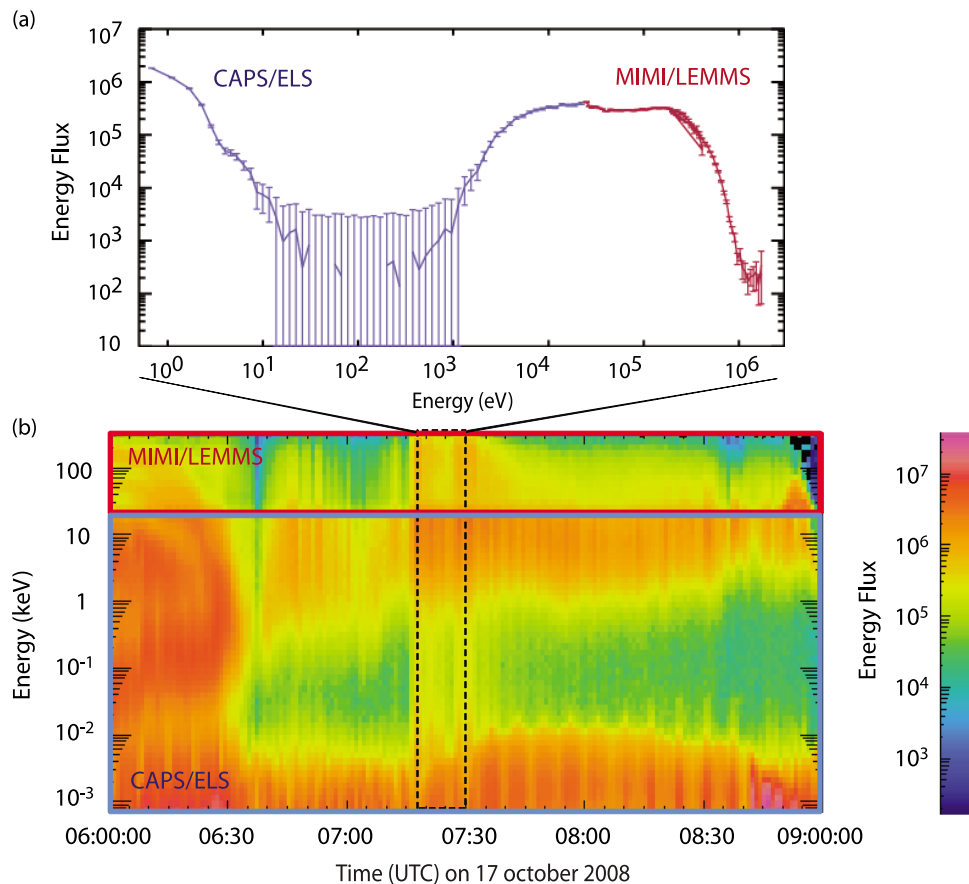


Figure B1. Composite CAPS/ELS and MIMI/LEMMS electron differential energy flux on 17 October 2008. (a) Spectral cut averaged between 0720 UT and 0730 UT. (b) Spectrogram in the 0600–0900 UT time interval.

of the analysis, as are the anisotropy in the hot electron temperature observed at the start of the interval.

Appendix B: MIMI/LEMMS Electron Observations

[76] The Low Energy Magnetospheric Measurements System (LEMMS) of the MIMI instrument [Krimigis *et al.*, 2004] is a solid state detector which measures electrons from 20 keV to 10 MeV, covering the energy range above CAPS. Figure B1 shows a CAPS/ELS-MIMI/LEMMS composite spectrogram (Figure B1b) in the 0600–0900 UT time interval and a spectral cut at 0720–0730 UT (Figure B1a). The MIMI/LEMMS detector was pointing to the 110°–90° pitch angle distribution from 0600 to 0800 UT. Anode 3 of the CAPS/ELS instrument was pointing roughly in the same direction (oscillating around 90°). Because the two instruments are not always looking in the same direction, and because of the background noise, a slight discontinuity appears at 15–20 keV (e.g., instrument overlapping energy range). Between 0600 UT and 0630 UT, electron flux in the MIMI/LEMMS energy range is high and is observed to form the tail of the suprathermal electron distribution function identified in the CAPS/ELS energy range. At 0630 UT, the energetic electron flux drops by a factor of 10, similarly to the

thermal (CAPS/ELS) electron flux. At 0720 UT, it is strongly enhanced up to 200 keV, indicating an important hardening of the electron spectra. Composite energy spectra (Figure B1a) shows that the electron population extends from a few keV to a hundred keV and displays equivalent energy flux in the whole energy range.

Appendix C: Cold Electron Density

[77] To place constraints on the presence of cold populations, we have analyzed the response of ELS to cold electron populations of varying density, following the modeling work of Arridge *et al.* [2009]. In this analysis synthetic spectra were constructed corresponding to Maxwellian distributions of varying densities and temperatures. In this we account for nonzero spacecraft potential (set to 19 V to match the observations in Figure 1) and the width of each ELS energy bin. These synthetic spectra were then subjected to a moment integration to determine the density and temperature. For accurately captured distributions the moment density and temperature should match the source Maxwellian density and temperature (see, e.g., Arridge *et al.* [2009] for more details). Figure C1 shows the ratio between the density (determined from a moment integration) and the source density as a function of the source Maxwellian temperature. Hence

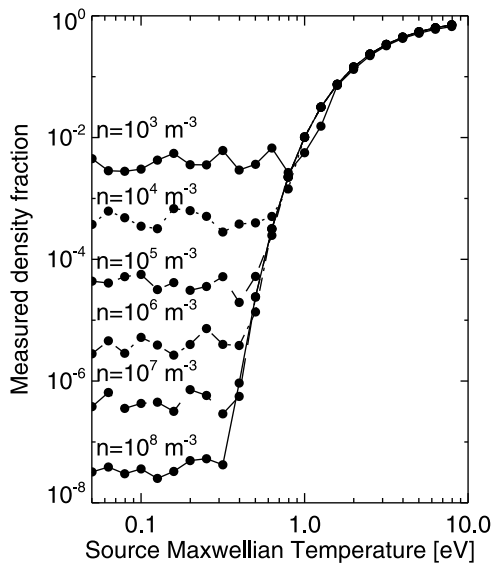


Figure C1. Ratio of the measured density to the real density as a function of Maxwellian temperature.

accurately measured spectra and moments would correspond to a fraction of 1.0 and should not display any temperature dependence. The multiple curves on Figure C1 correspond to different source Maxwellian densities. As can be seen the density fraction is a strong function of temperature. For ambient electron populations below around 0.8 eV the measured density is essentially decorrelated from the actual ambient electron density. Above this limit the measured density is an increasingly large fraction of the ambient density. There is some tendency for colder and denser electrons to be determined and essentially corresponds to the measurement of the high-energy tail of the Maxwellian. This analysis shows that if such cold plasma and cold plasma cavities are present in and around the SKR source region, they must have temperatures less than around 1 eV.

[78] Furthermore, one might expect such dense populations to have an observable effect on the charging of the spacecraft. In the inner magnetosphere there are electron populations with temperatures around 2 eV and number densities in excess of 10^7 m^{-3} which produce large charging currents that charge Cassini to negative potentials. The thermal charging current for a Maxwellian electron population with density n_e and temperature T_e is proportional to $n_e \sqrt{T_e}$ [e.g., Whipple, 1981]. Hence, cold high-latitude plasma populations where $n_e \sqrt{T_e} \approx \sqrt{2} \times 10^6 \text{ eV}^{1/2} \text{ m}^{-3}$ will be sufficient to produce measurable effects on the spacecraft potential. From the constraints developed above a very cold (0.1 eV) population with a number density of around $\sqrt{2}/0.1 \times 10^6 \approx \sqrt{2} \times 10^7$ would be sufficient to generate a significant charging effect on Cassini, but with an electron population essentially invisible to ELS. While a full charging simulation is required to properly investigate such an issue, such charging effects are not observed during this interval and suggest that such cold populations are not present. These arguments lead us to conclude that the SKR source region observed by Cassini on 17 October 2008 is devoid of cold plasma.

[79] **Acknowledgments.** The research at the University of Iowa was supported by the National Aeronautics and Space Administration through contract 1356500 with the Jet Propulsion Laboratory. C.S.A. was supported by an STFC Postdoctoral Fellowship in the United Kingdom. The research at LESIA and CESR was supported by the CNES agency. We thank RPWS, MAG, CAPS, and MIMI engineers for data reduction and software support. We thank the reviewers for commenting the paper.

[80] Masaki Fujimoto thanks Jan Hanzasz for his assistance in evaluating this paper.

References

- Andersson, L., R. E. Ergun, D. L. Newman, J. P. McFadden, C. W. Carlson, and Y. Su (2002), Characteristics of parallel electric fields in the downward current region of the aurora, *Phys. Plasmas*, *9*, 3600–3609, doi:10.1063/1.1490134.
- André, M., and T. Chang (1994), Ion heating perpendicular to the magnetic field, technical report, 41 pp., Cambridge Cent. for Space Res., Mass. Inst. of Technol., Cambridge.
- Arridge, C. S., L. K. Gilbert, G. R. Lewis, E. C. Sittler, G. H. Jones, D. O. Kataria, A. J. Coates, and D. T. Young (2009), The effect of spacecraft radiation sources on electron moments from the Cassini CAPS electron spectrometer, *Planet. Space Sci.*, *57*, 854–869, doi:10.1016/j.pss.2009.02.011.
- Benson, R. F., and W. Calvert (1979), Isis 1 observations at the source of auroral kilometric radiation, *Geophys. Res. Lett.*, *6*, 479–482, doi:10.1029/GL006i006p00479.
- Bunce, E. J., et al. (2008), Origin of Saturn's aurora: Simultaneous observations by Cassini and the Hubble space telescope, *J. Geophys. Res.*, *113*, A09209, doi:10.1029/2008JA013257.
- Bunce, E. J., et al. (2010), Extraordinary field-aligned current signatures in Saturn's high-latitude magnetosphere: Analysis of Cassini data during revolution 89, *J. Geophys. Res.*, *115*, A10238, doi:10.1029/2010JA015612.
- Carlson, C. W., et al. (1998), FAST observations in the downward auroral current region: Energetic upgoing electron beams, parallel potential drops, and ion heating, *Geophys. Res. Lett.*, *25*, 2017–2020, doi:10.1029/98GL00851.
- Chen, L., C. A. Kletzing, S. Hu, and S. R. Bounds (2005), Auroral electron dispersion below inverted-V energies: Resonant deceleration and acceleration by Alfvén waves, *J. Geophys. Res.*, *110*, A10S13, doi:10.1029/2005JA011168.
- Delory, G. T., R. E. Ergun, C. W. Carlson, L. Muschietti, C. C. Chaston, W. Peria, J. P. McFadden, and R. Strangeway (1998), FAST observations of electron distributions within AKR source regions, *Geophys. Res. Lett.*, *25*, 2069–2072, doi:10.1029/98GL00705.
- Dory, R. A., G. E. Guest, and E. G. Harris (1965), Unstable electrostatic plasma waves propagating perpendicular to a magnetic field, *Phys. Rev. Lett.*, *14*, 131–133, doi:10.1103/PhysRevLett.14.131.
- Dougherty, M. K., et al. (2004), The Cassini magnetic field investigation, *Space Sci. Rev.*, *114*, 331–383, doi:10.1007/s11214-004-1432-2.
- Elphic, R. C., et al. (1998), The auroral current circuit and field-aligned currents observed by FAST, *Geophys. Res. Lett.*, *25*, 2033–2036, doi:10.1029/98GL01158.
- Ergun, R. E., et al. (1998), FAST satellite wave observations in the AKR source region, *Geophys. Res. Lett.*, *25*, 2061–2064, doi:10.1029/98GL00570.
- Ergun, R. E., C. W. Carlson, J. P. McFadden, G. T. Delory, R. J. Strangeway, and P. L. Pritchett (2000), Electron-cyclotron maser driven by charged-particle acceleration from magnetic field-aligned electric fields, *Astrophys. J.*, *538*, 456–466, doi:10.1086/309094.
- Ergun, R. E., L. Andersson, D. S. Main, Y. Su, C. W. Carlson, J. P. McFadden, and F. S. Mozer (2002), Parallel electric fields in the upward current region of the aurora: Indirect and direct observations, *Phys. Plasmas*, *9*, 3685–3694, doi:10.1063/1.1499120.
- Gérard, J., B. Bonfond, J. Gustin, D. Grodent, J. T. Clarke, D. Bisikalo, and V. Schematovich (2009), Altitude of Saturn's aurora and its implications for the characteristic energy of precipitated electrons, *Geophys. Res. Lett.*, *36*, L02202, doi:10.1029/2008GL036554.
- Glauert, S. A., and R. B. Horne (2005), Calculation of pitch angle and energy diffusion coefficients with the PADIE code, *J. Geophys. Res.*, *110*, A04206, doi:10.1029/2004JA010851.
- Gorney, D. J., Y. T. Chiu, and D. R. Croley Jr. (1985), Trapping of ion conics by downward parallel electric fields, *J. Geophys. Res.*, *90*, 4205–4210, doi:10.1029/JA090iA05p04205.
- Gurnett, D. A., and L. A. Frank (1977), A region of intense plasma wave turbulence on auroral field lines, *J. Geophys. Res.*, *82*, 1031–1050, doi:10.1029/JA082i007p1031.
- Gurnett, D. A., et al. (2004), The Cassini radio and plasma wave investigation, *Space Sci. Rev.*, *114*, 395–463, doi:10.1007/s11214-004-1434-0.

- Horwitz, J. L. (1986), Velocity filter mechanism for ion bowl distributions (bimodal conics), *J. Geophys. Res.*, *91*, 4513–4523, doi:10.1029/JA091iA04p04513.
- Hultqvist, B. (1988), On the acceleration of electrons and positive ions in the same direction along magnetic field lines by parallel electric fields, *J. Geophys. Res.*, *93*, 9777–9784, doi:10.1029/JA093iA09p09777.
- Hultqvist, B., R. Lundin, K. Stasiewicz, L. Block, and P. Lindqvist (1988), Simultaneous observation of upward moving field-aligned energetic electrons and ions on auroral zone field lines, *J. Geophys. Res.*, *93*, 9765–9776, doi:10.1029/JA093iA09p09765.
- Kletzing, C. A., and S. Hu (2001), Alfvén wave generated electron time dispersion, *Geophys. Res. Lett.*, *28*, 693–696, doi:10.1029/2000GL012179.
- Klumpar, D. M., W. K. Peterson, and E. G. Shelley (1984), Direct evidence for two-stage (bimodal) acceleration of ionospheric ions, *J. Geophys. Res.*, *89*, 10,779–10,787, doi:10.1029/JA089iA12p10779.
- Knight, S. (1973), Parallel electric fields, *Planet. Space Sci.*, *21*, 741–750, doi:10.1016/0032-0633(73)90093-7.
- Kopf, A. J., et al. (2010), Electron beams as the source of whistler-mode auroral hiss at Saturn, *Geophys. Res. Lett.*, *37*, L09102, doi:10.1029/2010GL042980.
- Krimigis, S. M., et al. (2004), Magnetosphere Imaging Instrument (MIMI) on the Cassini Mission to Saturn/Titan, *Space Sci. Rev.*, *114*, 233–329, doi:10.1007/s11214-004-1410-8.
- Kurth, W. S., et al. (2011), A close encounter with a Saturn kilometric radiation source region, in *Planetary Radio Emissions VII*, Austrian Acad. of Sci., Vienna, in press.
- Lamy, L., et al. (2010), Properties of Saturn kilometric radiation measured within its source region, *Geophys. Res. Lett.*, *37*, L12104, doi:10.1029/2010GL043415.
- Lamy, L., B. Cecconi, P. M. Zarka, P. Canu, P. Schippers, W. S. Kurth, R. L. Mutel, D. A. Gurnett, D. Menietti, and P. Louarn (2011), Emission and propagation of Saturn kilometric radiation: Magnetoionic modes, beaming pattern, and polarization state, *J. Geophys. Res.*, *116*, A04212, doi:10.1029/2010JA016195.
- Linder, D. R., A. J. Coates, R. D. Woodliffe, C. Alsop, A. D. Johnstone, M. Grande, A. Preece, B. Narheim, and D. T. Young (1998), The Cassini caps electron spectrometer, in *Measurement Techniques in Space Plasmas: Particles*, *Geophys. Monogr. Ser.*, vol. 102, edited by R. F. Pfaff, J. E. Borovsky, and D. T. Young, pp. 257–262, AGU, Washington, D. C.
- Louarn, P., A. Roux, H. de Feraudy, D. Le Queau, and M. André (1990), Trapped electrons as a free energy source for the auroral kilometric radiation, *J. Geophys. Res.*, *95*, 5983–5995, doi:10.1029/JA095iA05p05983.
- Maggs, J. E. (1976), Coherent generation of VLF hiss, *J. Geophys. Res.*, *81*, 1707–1724, doi:10.1029/JA081i010p01707.
- Marklund, G. T. (2009), Electric fields and plasma processes in the auroral downward current region, below, within, and above the acceleration region, *Space Sci. Rev.*, *142*, 1–21, doi:10.1007/s11214-008-9373-9.
- Mauk, B. H., and J. Saur (2007), Equatorial electron beams and auroral structuring at Jupiter, *J. Geophys. Res.*, *112*, A10221, doi:10.1029/2007JA012370.
- Menietti, J. D., J. L. Burch, R. M. Winglee, and D. A. Gurnett (1993), DE 1 particle and wave observations in auroral kilometric radiation (AKR) source regions, *J. Geophys. Res.*, *98*, 5865–5879, doi:10.1029/92JA02340.
- Mitchell, D. G., W. S. Kurth, G. B. Hospodarsky, N. Krupp, J. Saur, B. H. Mauk, J. F. Carbary, S. M. Krimigis, M. K. Dougherty, and D. C. Hamilton (2009), Ion conics and electron beams associated with auroral processes on Saturn, *J. Geophys. Res.*, *114*, A02212, doi:10.1029/2008JA013621.
- Morgan, D. D., J. D. Menietti, R. M. Winglee, and H. K. Wong (2000), Perpendicular electron heating by absorption of auroral kilometric radiation, *Planet. Space Sci.*, *48*, 41–49, doi:10.1016/S0032-0633(99)00079-3.
- Mutel, R. L., J. D. Menietti, D. A. Gurnett, W. Kurth, P. Schippers, C. Lynch, L. Lamy, C. Arridge, and B. Cecconi (2010), CMI growth rates for Saturnian kilometric radiation, *Geophys. Res. Lett.*, *37*, L19105, doi:10.1029/2010GL044940.
- Pritchett, P. L., and R. J. Strangeway (1985), A simulation study of kilometric radiation generation along an auroral field line, *J. Geophys. Res.*, *90*, 9650–9662, doi:10.1029/JA090iA10p09650.
- Roux, A., A. Hilgers, H. de Feraudy, D. le Queau, P. Louarn, S. Perraut, A. Bahnsen, M. Jespersen, E. Ungstrup, and M. André (1993), Auroral kilometric radiation sources: In situ and remote observations from Viking, *J. Geophys. Res.*, *98*, 11,657–11,670, doi:10.1029/92JA02309.
- Rymer, A. M., B. H. Mauk, T. W. Hill, C. Paranicas, D. G. Mitchell, A. J. Coates, and D. T. Young (2008), Electron circulation in Saturn's magnetosphere, *J. Geophys. Res.*, *113*, A01201, doi:10.1029/2007JA012589.
- Sagdeev, R. Z., and A. A. Galeev (1966), Non-linear plasma theory, *Tech. Rep. IC/66/64*, Int. Centre for Theoret. Phys., Trieste, Italy.
- Schippers, P., et al. (2008), Multi-instrument analysis of electron populations in Saturn's magnetosphere, *J. Geophys. Res.*, *113*, A07208, doi:10.1029/2008JA013098.
- Sittler, E. C., Jr., K. W. Ogilvie, and J. D. Scudder (1983), Survey of low-energy plasma electrons in Saturn's magnetosphere: Voyagers 1 and 2, *J. Geophys. Res.*, *88*, 8847–8870, doi:10.1029/JA088iA11p08847.
- Strangeway, R. J., et al. (1998), FAST observations of VLF waves in the auroral zone: Evidence of very low plasma densities, *Geophys. Res. Lett.*, *25*, 2065–2068, doi:10.1029/98GL00664.
- Talboys, D. L., C. S. Arridge, E. J. Bunce, A. J. Coates, S. W. H. Cowley, and M. K. Dougherty (2009a), Characterization of auroral current systems in Saturn's magnetosphere: High-latitude Cassini observations, *J. Geophys. Res.*, *114*, A06220, doi:10.1029/2008JA013846.
- Talboys, D. L., C. S. Arridge, E. J. Bunce, A. J. Coates, S. W. H. Cowley, M. K. Dougherty, and K. K. Khurana (2009b), Signatures of field-aligned currents in Saturn's nightside magnetosphere, *Geophys. Res. Lett.*, *36*, L19107, doi:10.1029/2009GL039867.
- Ungstrup, E., A. Bahnsen, H. K. Wong, M. André, and L. Matson (1990), Energy source and generation mechanism for auroral kilometric radiation, *J. Geophys. Res.*, *95*, 5973–5981, doi:10.1029/JA095iA05p05973.
- Whipple, E. C. (1981), Potentials of surfaces in space, *Rep. Prog. Phys.*, *44*, 1197–1250, doi:10.1088/0034-4885/44/11/002.
- Winglee, R. M., and P. L. Pritchett (1986), The generation of low-frequency electrostatic waves in association with auroral kilometric radiation, *J. Geophys. Res.*, *91*, 13,531–13,541, doi:10.1029/JA091iA12p13531.
- Wu, C. S., and L. C. Lee (1979), A theory of the terrestrial kilometric radiation, *Astrophys. J.*, *230*, 621–626, doi:10.1086/157120.
- Wu, C. S., H. K. Wong, D. J. Gorney, and L. C. Lee (1982), Generation of the auroral kilometric radiation, *J. Geophys. Res.*, *87*, 4476–4487, doi:10.1029/JA087iA06p04476.
- Young, D. T., et al. (2004), Cassini Plasma Spectrometer investigation, *Space Sci. Rev.*, *114*, 1–112, doi:10.1007/s11214-004-1406-4.
- Young, D. T., et al. (2005), Composition and dynamics of plasma in Saturn's magnetosphere, *Science*, *307*, 1262–1266, doi:10.1126/science.1106151.

N. André and S. Grimald, Centre d'Étude Spatiale des Rayonnements, Université de Toulouse, UPS, 9 av. Colonel Roche, F-31028 Toulouse CEDEX 9, France.

C. S. Arridge and A. J. Coates, Mullard Space Science Laboratory, University College London, Holmbury St. Mary RH5 6NT, UK.

B. Cecconi, LESIA, CNRS, Observatoire de Meudon, 5 place J. Janssen, F-92190 Meudon CEDEX, France.

M. K. Dougherty and L. Lamy, Department of Space and Atmospheric Physics, Imperial College, Prince Consort Road, London SW7 2BZ, UK.

D. A. Gurnett, W. S. Kurth, J. D. Menietti, and P. Schippers, Department of Physics and Astronomy, University of Iowa, 710 Van Allen, Iowa City, IA 52240, USA. (patricia-schippers@uiowa.edu)

N. Krupp, Max-Planck-Institut für Sonnensystemforschung, Max-Planck-Str. 2, D-37191 Katlenburg-Lindau, Germany.

D. G. Mitchell, Applied Physics Laboratory, Johns Hopkins University, MP3-E132, 11100 Johns Hopkins Rd., Laurel, MD 20723, USA.

D. T. Young, Space Science and Engineering Division, Southwest Research Institute, 6220 Culbena Dr., San Antonio, TX 78238-0000, USA.